Lawrence Berkeley National Laboratory

Title
Simulating the Effects of Surface Energy Partitioning on Convective Organization: Case Study and Observations in the US Southern Great Plains

Permalink
https://escholarship.org/uc/item/2bd9t8wr

Journal

ISSN

Authors
Dai, Yi
Williams, Ian N
Qiu, Shaoyue

Publication Date
2021-01-27

DOI

Peer reviewed

1 **Simulating the effects of surface energy partitioning on convective organization: Case**
2 **study and observations in the US Southern Great Plains**
3
4 Yi Dai[1], Ian N. Williams[1,2], and Shaoyue Qiu[1]
5
6 1 Climate and Ecosystem Sciences Division, Lawrence Berkeley National Laboratory, Berkeley,
7 CA, USA
8 2 Department of Geological and Atmospheric Sciences, Iowa State University
9
10 Corresponding author: Yi Dai (yidai@lbl.gov)
11
12 **Key points**
13

14 - Wet soil can lead to better organized convection than dry, constituting a positive rainfall
15   feedback, despite earlier triggering over dry
16 - Cold pools diminish or contribute to feedback; their effects vary with convective lifecycle
17   stage and are not captured in parameterizations
18 - Enhanced surface latent heat flux along gust fronts provides additional positive feedback
19   that may help convection persist after sunset

20   **Abstract**
21   Realistic cloud-resolving simulations were performed to study the effects of surface energy
22   partitioning (surface sensible and latent heat fluxes) on the organization of isolated convection
23   into larger mesoscale convective systems (MCSs) near the US Southern Great Plains. The role of
24   cold pools in mediating surface-convection interactions was explored. Better organized MCSs
25   tended to occur in the experiments with perturbed wetter soil (and more active vegetation),
26   regardless of the effects of soil moisture on the diurnal timing of convective triggering. Wetter
27   soil led to shallower boundary layers and more convective available potential energy than drier
28   soil. The roles of cold pools on convection are lifecycle-stage dependent: A dry surface allows
29   more numerous colliding cold pools, thereby aiding in convective triggering by reducing
30   entrainment in the early stages, and providing gust-front uplift in later stages. However,
31   horizontal propagation of the cold-pool density current can outrun the convective system,
32   creating a slantwise updraft and thus weakening the gust front uplift in later stages. This effect
33   calls into question previous cold pool parameterizations, in which the gust front uplift is mainly
34   proportional to the negative buoyancy of cold air. Lastly, both the model and observation show
35   an enhancement of surface latent heat flux during the passage of a gust front at night, suggesting
36   that a positive feedback between the surface and convection helps MCSs to persist into the
37   nighttime.

38
39   **Plain Language Summary**
40   Numerical simulations explicitly resolving thunderstorms were used to study the effects of the
41   land surface (soil moisture/vegetation) on rainfall in the US South Great Plains. Better
42   convective organization (larger, stronger thunderstorm clusters with heavier rainfall) occurred
43   more often in perturbed wetter soil/vegetation experiments than in dry experiments, indicating a
44   positive feedback of soil moisture on rainfall. A case study was conducted to explore the
45   mechanism of this feedback. Although dry soil is initially more favorable for triggering
46   thunderstorms, wetter soil can modify environmental conditions (convective available potential
47   energy) to become more favorable for further development of isolated thunderstorms into larger
48   organized clusters. Current climate models do not fully capture the feedback mechanisms
49   indicated here. The results provide insight into how climate models can be improved to more
50   realistically represent processes connecting rainfall to future land-surface change.

51
52   **1. Introduction**
53   Evapotranspiration not only directly provides water vapor for precipitation, it also influences
54   convective precipitation by changing atmospheric dynamics and stability (Schar et al., 1999).
55   The interaction of convection with the land surface is complicated because it depends on the
56   lifecycle stage of convective precipitation—isolated convective cells are initially triggered, but
57   can grow upscale into organized clusters. Atmospheric state-dependence, spatial heterogeneities
58   in soil and vegetation, and spatial and temporal scale dependence (Guillod et al. 2015) add
59   further complexity. For example, modeling (e.g., Findell & Eltahir 2003a; Williams, 2019;
60   Konings et al., 2010; Gentine et al., 2013; Yin et al., 2015) and observational studies (Qiu and
61   Williams, 2020) have shown that whether a wet or dry surface is more favorable for triggering
62   convection depends mainly on the early-morning low-level temperature (stratification) and
63   humidity structure. Specifically, convection is more easily triggered over dry soil and heat
64   surface sensible heating, when the rapidly growing planetary boundary layer (PBL)
65   overcompensates the increase of the level of free convection (LFC) due to a drier atmosphere,

66 causing a negative feedback. Yet the sign of the feedback on precipitation may change from
67 negative to positive after convection is triggered and organized (e.g., Gantner & Kalthoff, 2010;
68 Froidevaux et al., 2014).
69   Convective organization is an important process in the water cycle, because once
70 convective cells are organized, the system is more likely to persist and produce more rainfall.
71 Organized convective clouds are often referred to as mesoscale convective systems (MCSs)
72 when their precipitation region exceeds 10,000 km^2, or is over 100 km in at least one dimension
73 (Houze 2004). MCSs are a major source of summertime extreme weather and precipitation in
74 continental climates (Fritsch et al., 1986; Feng et al., 2016), including over the US Southern
75 Great Plains (SGP) where our study is based. The failure of climate models in capturing
76 convective organization contributes to the erroneous diurnal timing of summer precipitation and
77 covnective clouds over land at midday instead of the observed late afternoon and night (e.g., Dai
78 et al., 1999; Yang & Slingo, 2001; Pfeifroth et al., 2012; Yin et al., 2020).
79   Cloud-resolving models can simulate a positive feedback of soil moisture on convection
80 in the mature stage of organized convective systems in real-case studies (e.g., over West Africa;
81 Gantner & Kalthoff, 2010). Whether such feedbacks work in other environments, and by what
82 mechanisms, are fundamental questions for reducing uncertainties in drought and heavy
83 precipitation projections (e.g., Zeng et al., 2019). Findell and Eltahir (2003a) did not address the
84 question of convective organization as their boundary layer model was switched off as soon as
85 convection was triggered. Schar et al. (1999) found more precipitation in perturbed wet soil
86 experiments in a regional climate model with convective parameterization, primarily because the
87 wet soils led to a shallower boundary layer and a build-up of convective available potential
88 energy (CAPE). Hohenegger et al. (2009) found a different result from Schar et al. (1999): in the
89 coarse-resolution climate model, the results were similar to Schar et al. (1999), in that wet soils
90 ensure more precipitation; however, in the cloud-resolving model, the dry soil led to more
91 precipitation. Although a particular condition (a stable layer on top of the PBL) exists in
92 Hohenegger et al. (2009), the spatial resolution is no doubt a key difference. Therefore, in this
93 paper we use a cloud resolving model to explore land-surface feedback on convective
94 organization.
95   A major advantage of cloud-resolving models is their ability to resolve the convection-
96 coupled cold pool which results from the combination of cooling by evaporation of precipitation,
97 the downward drag effect of falling hydrometers, and downward dynamic pressure gradient force
98 in convective updrafts. Cold pools are thought to play important roles in convective organization.
99 The cold pool can thermodynamically support new convection by creating cold and moist air
100 within the edge of the cold pool (e.g., Tompkins, 2001; Torri et al., 2015). The CAPE is
101 increased and the convective inhibition (CIN) is decreased along the edge of the cold pool.
102 Another mechanism is the ascent within the narrow surface gust front zone caused by
103 convergence of the cold-pool air and environmental air (e.g., Rotunno et al., 1988; Jeevanjee &
104 Romps, 2015; Torri et al., 2015). By creating larger convergence near the gust fronts, cold pools
105 whose propagation and strength are dynamically balanced with environmental shear might aid in
106 organizing convection (Rotunno et al., 1988). Moreover, colliding cold pools help create larger
107 clouds (Feng et al., 2015; Haerter et al., 2019), which have lower entrainment rates than smaller
108 clouds (e.g., Kuang & Bretherton, 2005; Khairoutdinov & Randall, 2006; Schlemmer &
109 Hohenegger, 2014), favoring stronger convection. Stronger convection might in turn create
110 stronger gust fronts, and a positive feedback on convective organization.

111   The cold pool could be a natural agent in connecting the land surface with convective
112   organization. Hypothesized mechanisms for this connection can be grouped into three broad
113   categories, involving cloud entrainment, stability (CAPE), and surface flux interactions. First,
114   cold pool dynamics could link the convective triggering feedback and convective organization
115   via cloud entrainment. For example, a drier surface could produce deeper boundary layers,
116   triggering more numerous isolated convective cells and thus more intersecting cold pools than a
117   wetter surface; leading to wider convective clouds, reduced entrainment, and better convective
118   organization. On the other hand, over wet soils where shallow boundary layers can accumulate
119   CAPE, convergence along gust fronts could provide a mechanism to lift the unstable air to the
120   LFC (Froidevaux et al., 2014), producing a positive soil moisture-precipitation feedback
121   analogous to that in climate models which lack cold pool dynamics (Schar et al., 1999). Those
122   models parameterized convection as a function of CAPE, and thus may correctly capture the soil
123   moisture-CAPE relationship in some cases for the wrong physical reason (e.g., Hohenegger et al.
124   2009), which warrants further study here. Lastly, when the cold and unsaturated downdraft air in
125   the cold pools contacts the surface, both the surface sensible and latent heat fluxes will change
126   due to the temperature and moisture difference between the land surface and near-surface
127   atmosphere, as well as due to the increased wind speed associated with the gust fronts. If the
128   location of the enhanced surface fluxes is close to the location of the newly triggered convection
129   (near the gust front), we can expect that organized convection will persist into the nighttime.
130   Adding cold pool parameterizations to climate models has led to improved convective
131   precipitation over land (Rio et al., 2009; Grandpeix & Lafore, 2010) and ocean (Del Genio et al.,
132   2015), in terms of the diurnal cycle and amount. However, potential interactions of cold pools
133   with the land-surface, noted above, are not yet taken into account. Moreover, these interactions
134   have been investigated mainly in idealized small-domain cloud resolving models or large eddy
135   simulations (LESs), without resolving the full spatial scale of realistic organized convective
136   systems or MCSs. The motivation of this paper is threefold. First, we want to investigate how
137   land surface fluxes affect the convective organization in real case experiments using a cloud
138   resolving model. Second, we want to test hypothesized cold pool effects on convective
139   organization as suggested by smaller-domain studies. Finally, we are hoping to have some
140   insights into the cold pool and convective parameterizations for global models.
141
142   **2. Methodology**
143
144   **2.1. Model description**
145   The Weather Research and Forecasting (WRF, version 3.8.1, Skamarock et al., 2008) model was
146   used to simulate realistic MCSs near the SGP site. The simulated domain contained 454 x 600
147   grid points with horizontal grid spacing of 3 km, over a region from about 28° N 42° N
148   meridionally, and 105° W to 92°W zonally. Vertically, layer thickness gradually increased from
149   about 50 m near the surface to 400 m at z = 2500 m, and was constant at about 750 m upward to
150   the model top at around 20,000 m. The 6-h North American Mesoscale Forecast System (NAM,
151   12-km horizontal resolution, available from March 2004 to present) was used for both the initial
152   condition and lateral boundary condition.
153   Table 1 shows the model physics schemes used in this study. No cumulus scheme was
154   used because the 3-km horizontal resolution is able to resolve clouds. The RRTMG scheme
155   (Iacono et al., 2008) was used for both shortwave and longwave radiation. We have chosen the
156   Thompson scheme (Thompson et al., 2008) for microphysics, because comparison of different

157   microphysics schemes in test experiments (not shown) indicated that the Thompson scheme was
158   better to represent the MCS cloud field than other schemes. The MYNN level 2.5 scheme
159   (Nakanishi & Niino, 2009) was used for the planetary boundary layer.
160   The Community Land Model Version 4 (CLM4, Lawrence et al., 2011) was used for land
161   surface parameterization, with modifications described below. Although newer versions of CLM
162   are available, CLM4 was the latest supported version coupled to WRF (Lu & Kueppers, 2012) at
163   the start of our study. For this study, modifications were made to CLM4 in WRF to better
164   represent the land surface in the Southern Great Plains (as described in Williams et al. 2020).
165   Notably, stomatal and soil resistance parameters were changed to better represent surface energy
166   partitioning compared to observations, and higher-resolution input soil and vegetation datasets
167   were used. The latter include a new plant functional type and leaf area index dataset developed to
168   capture the heterogeneous distribution of winter crops and grasses across much of Oklahoma and
169   Kansas. WRF-CLM was initialized with a spun-up offline run of CLM forced with
170   meteorological data including 4 km gridded hourly precipitation data combining WSR-88D
171   NEXRAD radar and rain gauge estimates (see Williams et al. 2020).

172
173   Table 1. Model physics schemes used in this study

WRF physics schemes	
Radiation (longwave and shortwave)	RRTMG (Iacono et al., 2008)
Microphysics	Thompson scheme (Thompson et al. 2008)
PBL	MYNN level-2.5 (Nakanishi & Niino, 2009)
Land surface model	CLM4 (Lawrence et al. 2011)

174
175   **2.2. Study site and selection of MCS cases**
176   MCSs can originate as surface-based isolated convective clouds (cumulonimbus), which often
177   organize over the US High Plains and propagate over the SGP at night in concert with the
178   nocturnal low-level jet. However, it is not unusual for MCSs to develop from isolated convection
179   over the SGP as well. Of these, we are particularly interested in cases of weak synoptic forcing,
180   in which the land surface could have greater influence. Weakly forced cases are also of interest
181   as they pose a greater challenge for numerical forecast models (Squitieri and Gallus, 2016). We
182   focused on events triggered near the US Department of Energy Atmospheric Radiation
183   Measurement (ARM) site, which includes a dense network of surface and atmospheric profiling
184   measurements over Northern and Central Oklahoma and Southern Kansas. The long-term
185   operation of this network from approximately 1999 to present allowed several cases to be
186   selected in contrasting environments, as described below.
187   We used the Geostationary Operational Environmental Satellite (GOES, Minnis et al.
188   2008) data (4 km spatial resolution and 30-minute temporal resolution) to identify events in
189   which afternoon (12:00-18:00 LST) convection is triggered and subsequently organized near the
190   SGP site. Details are provided in Qiu and Williams (2020) and briefly summarized here. A cloud
191   system was defined by contiguous cloudy pixels in the GOES visible cloud mask data. Events
192   that were initiated from isolated cumulonimbus were separated from propagating events initiated
193   outside the SGP region, based on size and time evolution (events were required to start as
194   isolated deep cumulus and grow in excess of 100 km x 100 km). From this larger sample, we
195   removed cases by visual inspection that were associated with strong frontal boundaries (to focus
196   on surface influences) and removed cases that did not have contiguous precipitation extending
197   over 100 km in at least one direction (using the Next Generation Weather Radar [NEXRAD]

198 reflectivity). Note that our selection of MCSs included both cases that are organized into
199 compact clusters with strong convective cells, and those that cover a large region but with
200 relatively weak and scattered multicellular cells (to be shown in Fig. 1 and Fig. S1, S2).
201   To further narrow the cases a computationally feasible sample size most relevant to our
202 hypotheses (three mechanisms in the Introduction), we chose cases in the wettest and driest
203 quartiles of morning (09:00-12:00 LST) surface evaporative fraction (defined as the ratio of
204 latent heat flux to the sum of latent and sensible heat flux) over a 3° x 3° domain centered over
205 the ARM Central Facility, based on surface flux measurements (Tang et al. 2019). The
206 evaporative fraction was used because latent heat and sensible fluxes can also be influenced by
207 net radiation. Of the drier cases, we required that the morning (07:00 LST) lower-tropospheric
208 relative humidity and thermal stratification be in the negative 'triggering feedback' regime or so-
209 called 'dry-soil-advantage' regime as defined earlier (e.g., Qiu and Williams, 2020; Williams,
210 2019; Findell and Eltahir, 2003a), and likewise for the wettest quartile we selected those in the
211 positive triggering feedback regime. As noted in the introduction, over a land surface with low
212 evaporative fraction (high sensible heating) and in tropospheric states where the rapidly growing
213 planetary boundary layer (PBL) can overcompensate for the increase of the LFC due to a drier
214 PBL, a negative 'triggering feedback' on convective triggering occurs; i.e., negative soil
215 moisture anomalies are more likely to trigger deep convection. On the other hand, a positive
216 feedback is hypothesized when moistening of the low-level atmosphere brings the LFC down to
217 the PBL top, preferentially triggering convection over wet soil or actively transpiring vegetation.
218 While regime-based selection does not guarantee cases in which MCS development will exhibit
219 sensitivity to surface forcing, it provides a practical starting point for case selection given the
220 computational infeasibility of simulating all MCS cases.
221   A total of 14 cases (9 in negative feedback regime and 5 in the positive regime) were
222 chosen and simulated. Dates for negative regime cases were 2006-08-10, 2011-07-02, 2011-07-
223 12, 2011-07-24, 2011-08-06, 2011-08-24, 2012-05-29, and 2012-07-19. Dates for the positive
224 regime were 2007-06-19, 2007-07-04, 2007-07-14, 2015-07-20, and 2007-08-02. After exploring
225 common features across cases, we focused on one typical case to test the detailed hypotheses
226 noted above, and to allow for additional experiments on the role of cold pools.
227
228 **2.3. Perturbed WET and DRY surface condition**
229 The effect of surface energy partitioning in this paper is realized by perturbing the soil moisture.
230 As described above, a spun-up offline run of CLM was used to provide land surface initial
231 conditions for WRF in which soil moisture reflects observed meteorological forcing and thus
232 represents real hindcast days. We hereafter refer to these simulations as the 'control' or CTL. To
233 explore the impacts of the hydrologic state of the land surface on convective organization, two
234 additional experiments were performed in which soil moisture was initialized higher and lower
235 than the reference (WET and DRY experiments, respectively). The perturbed high and low
236 values were defined by the maximum and minimum values of the model daily summer (June-
237 August) climatology (2000-2016), defined per grid cell and soil vertical level. These
238 perturbations are plausible yet large enough for exploring the general effect of wet versus dry
239 surface conditions on convection (e.g., as opposed intraseasonal variability in monthly soil
240 moisture anomalies from climatology; Koster et al. 2003). In CLM4, the soil solumn is 42 m
241 deep, but for grasses and C3 crops about 90% of the root fraction is in the top 0.83 m of the soil
242 column, which can be considered the relevant 'surface' soil depth with respect to
243 evapotranspiration from a vegetated surface. The upper 10 layers received the soil moisture

244   perturbation, with the top layer between 0-1.8 cm, and bottom layer between 229.6-380.2 cm
245   (Lawrence et al. 2011).
246   Our experiments were designed to explore the response of convection to relatively
247   homogeneously dry or wet surface conditions in which the convective boundary layer is deep or
248   shallow over a large area. The area of the soil moisture perturbation was confined to a circle of
249   diameter 500 km (on the order of the internal Rossby radius of deformation), centered over the
250   SGP site. To avoid a sharp discontinuity in soil moisture, perturbations were tapered to 0 linearly
251   over an extended region 350 km outward from the edge of the circular perturbation. With this
252   smooth gradation in soil moisture, we did not observe gravity waves or secondary circulations
253   associated with the edge of the perturbed region. Note that our deliberate focus on large-scale
254   anomalies in surface energy partitioning (as opposed to smaller mesoscale heterogeneity or
255   landscape 'patchiness') is motivated by the fact that many convective parameterizations (with
256   CAPE-based trigger functions) still do not realistically couple convective triggering to boundary
257   layer turbulence, which can provide a lifting mechanism to overcome convective inhibition
258   energy regardless of whether the turbulence is driven by a horizontally homogeneous or
259   heterogeneous surface (e.g., Williams, 2019). Moreover, such large-scale soil moisture (and
260   vegetation state) anomalies are common during major droughts and pluvial events.
261   Our intent in performing the WET and DRY experiments is not to quantify soil moisture
262   effects per se, but to explore how convection responds to variations in surface evaporative
263   fraction. To achieve this goal, it is necessary to consider the physical properties of soil and
264   vegetation that may limit evapotranspiration even if the soil column is near saturation. For this
265   reason, our WET configuration was additionally modified to have reduced stomatal and soil
266   resistances to evapotranspiration. Specifically, we reduced the leaf-litter layer resistance by a
267   factor 0.5, and increased the stomatal conductance by a factor of 2. The latter helped raise the
268   upper limit on transpiration that is imposed by model vegetation, and was implemented after
269   initial tests revealed vegetated areas with muted responses of latent heat flux when WET was
270   configured using soil moisture perturbations alone. The result of these modifications is that WET
271   represents a land surface with actively transpiring vegetation, ample soil moisture supply, and
272   reduced leaf-litter impedance of bare soil evaporation. The comparison of simulations before and
273   after the stomatal and soil resistance modifications are shown in Fig. S1c. Overall, these
274   modifications help to create a larger difference between DRY and WET simulations.
275
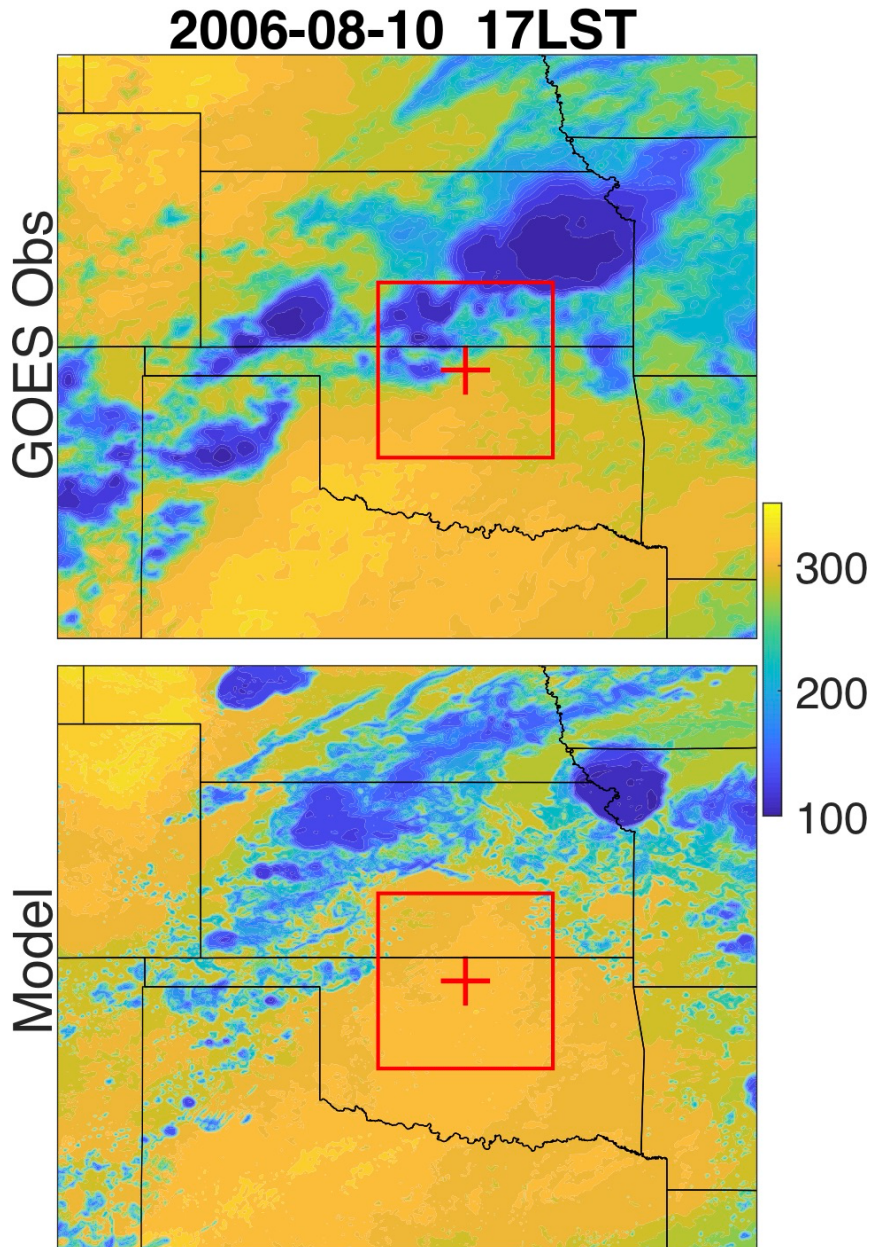
276
277   Figure 1. Comparison of OLR (W/m2) between the GOES observation (upper panel) and model data (lower panel),
278   for case 2006-08-10 at 17:00 LST near the SGP site (red cross: 36.6 N, 97.5 S). Red box indicates 3º X 3º domain
279   centered at the SGP site.
280

281   **3. General behavior of simulations**
282   **3.1. Validity of simulated MCSs**
283   We first verified how well the chosen cases are captured by control (CNT) simulations.
284   Snapshots of the outgoing longwave radiation (OLR) for both the simulations and the
285   Geostationary Operational Environmental Satellite (GOES) data are used to compare case 2006-
286   08-10 in Fig. 1. The comparisons of all the other 13 cases are shown in Fig. S1 and S2. The
287   model seems to show smaller convective-scale features, compared to the observation. Overall,
288   the model is quite good at capturing the observed deep convective cloud field, although some
289   spatial and temporal displacements exist. In a few cases, such as 2011-07-30, 2007-08-02, and

290   2007-06-19, parts of the convective feature are not simulated; also, case 2007-06-19 has a lagged
291   (about 3 hours) convective response in the model compared to observation. We choose to keep
292   those cases, because model sensitivity to soil moisture (which is the main focus of this paper) in
293   those cases is large. The difference between model and observations in those cases also indicates
294   the difficulty in simulating the weakly forced MCSs. We note that initial condition sensitivity
295   tests (varying the model initialization time between 00:00, 06:00, and 12:00 UTC) did not
296   significantly change the location and timing of convection, and for brevity we discuss results
297   initialized at 06:00 UTC.

298
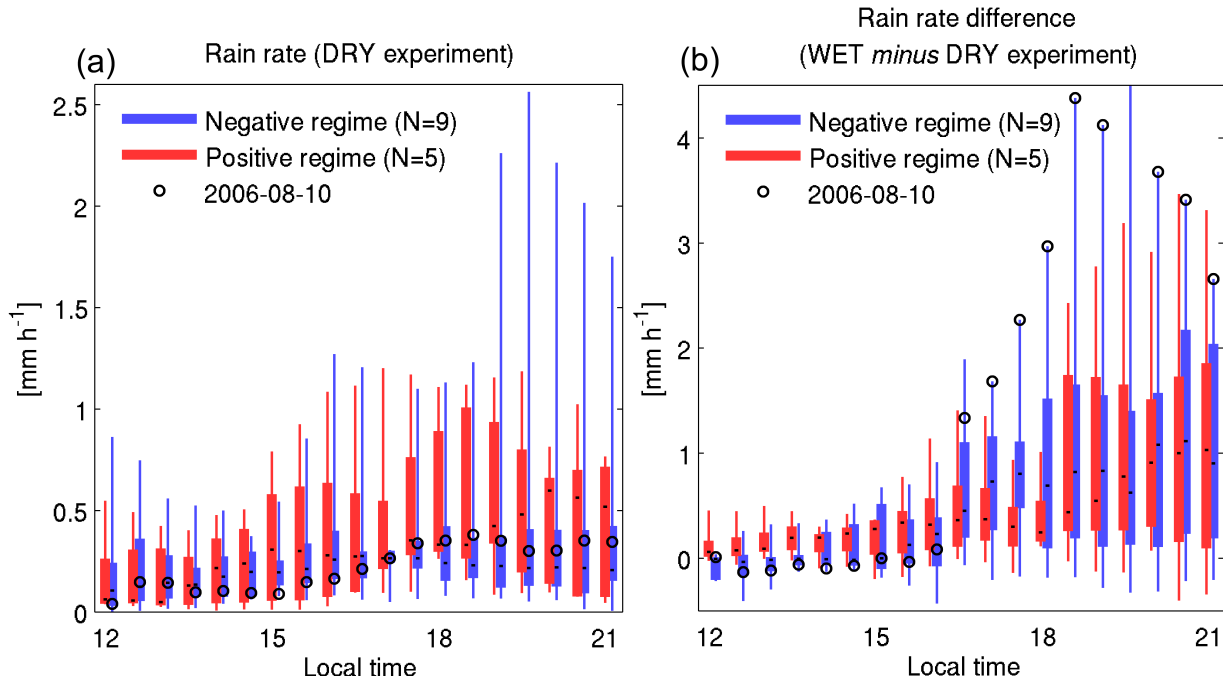
299
300   Figure 2. Half-hourly rain rate (spatial average, 600km X 600km centered at SGP site) for cases in positive (red) and
301   negative (blue) triggering feedback regimes. Black notches, shaded bars, and lines indicate the median, interquartile
302   range, and extrema, respectively. Positive and negative regime results are slightly offset to aid visualization.

303
304   **3.2. WET *VS* DRY simulations**
305   Next, we compared the increased soil moisture (WET) and decreased soil moisture (DRY)
306   experiments. Fig. 2 shows the time series of the area-mean rain rate for DRY (Fig. 2a) and the
307   difference between WET and DRY (Fig. 2b), in a statistical way for all the negative and positive
308   regime cases. To be consistent with the criterion used in choosing cases, we chose the area that is
309   centered in the SGP site, with a size of 600 km by 600 km in order to include MCSs that might
310   have some location difference from observed ones. In DRY experiments (Fig. 2a), late afternoon
311   and early evening (around 16:00-20:00 LST) have slight preference for higher rain rates than
312   other times, although large variations exist across simulations. Overall, rain rate is low for all
313   cases in DRY simulations. In contrast, WET simulations generally have a higher rain rate than
314   DRY regardless of triggering feedback regime (note that y-axis scale in Fig. 2b is larger than Fig.
315   2a). For most negative regime cases, rain rate in WET is slightly weaker than DRY before about
316   16:00 LST; for positive regime cases rain rate in WET is much higher than DRY before 16:00
317   LST, consistent with the regime-dependent triggering feedback hypothesis discussed above (dry
318   soil is more favorable for triggering convection in the negative regime). However, later on, much
319   larger rain rate occurs in WET compared to DRY even in negative regime cases, and this trend

320   persists until the end of simulations. For positive regime cases, WET always has a larger rain rate
321   than DRY for the whole time period. The takeaway message in Fig. 2 is that, in most simulated
322   cases, WET has a larger rainfall rate than DRY in the late afternoon or early evening (although
323   large variation exists across simulations), regardless of the initial influence of the surface
324   perturbation on triggering. It is noteworthy that not every case shows such a feature. In the
325   negative regime case of 2011-08-24, the WET experiment has almost no rain or convection
326   during the whole simulation, due to a very stable boundary layer that does not allow convection
327   to initiate over the wetter surface. We conclude that while evapotranspiration can sometimes
328   determine whether organized convection develops at all, in most of our cases the influence of the
329   surface on triggering is dominated by its positive influence on the later stages of organization.
330
331   **4. 2006-08-10 case**
332   **4.1 Gust fronts and convective cells**
333   We chose the 2006-08-10 case (black circles in Fig. 2) to evaluate in detail the three mechanistic
334   hypotheses of cold pool-mediated surface influences on convective organization described in the
335   introduction (involving surface fluxes, CAPE, and cloud entrainment). To do so we compared
336   the behavior of cold pools, gust fronts, and cloud cell size between WET and DRY. Compared
337   with other cases, 2006-08-10 is representative of a fairly typical case that is neither
338   extraordinarily strong, nor in a particularly favorable environment (with a moderate CAPE of
339   about 1000 J/kg). However, it also exhibits the switch in feedback suggested in earlier studies,
340   from an initially negative triggering feedback to a positive feedback on rain rate at the mature
341   stage. In particular, we focus on understanding the much greater mature-stage rain rate in WET
342   despite earlier triggering in DRY. Before presenting the detailed results, we first present the
343   surface energy partitioning for 2006-08-10 CTL, DRY, and WET, respectively in Figure S1.
344   Evaporative fraction (EF) is used to show the surface energy partitioning. EF does not change
345   much from morning to mid-afternoon (Fig. S1a): in both of CTL and DRY, EF is small at around
346   0.2 (with slight larger value in CTL), indicating that the sensible heating is leading the surface
347   fluxes. On the contrary, EF in WET is close to 1, meaning that the latent heating is much larger
348   than sensible heating.
349   Gust fronts are the enhanced near-surface wind created by cold pool downdrafts. They
350   are located near the edge of cold pools where low-level wind and density show discontinuity.
351   Based on air continuity, gust fronts in this paper are visualized by positive vertical velocity in the
352   lower boundary layer. A comparison of boundary layer gust fronts between DRY and WET
353   experiments (Fig. 3) shows that numerous small convection-induced gust fronts exist early in the
354   convective triggering stage at 14:00 LST in DRY (Fig. 3a), while there are almost no gust fronts
355   in WET at that time (Fig. 3d). As stated above, the 2006-08-10 case falls within the negative (dry
356   advantage) regime, in which convective triggering is hypothesized to occur more readily over a
357   drier surface having higher sensible heat flux (SH). Indeed, these results suggest more numerous
358   colliding gust fronts and a possible pathway for a dry surface to influence convective
359   organization in favorable environments. Note that the line-type positive and negative vertical
360   velocities prevalent in Fig. 3a are convective rolls driven by turbulence in the planetary boundary
361   layer. In DRY, sensible heating is much higher than WET in the afternoon, creating a very active
362   turbulent boundary layer. This feature nearly occurs in every DRY simulation, and it is not
363   sensitive to planetary boundary layer parameterizations (results not shown in figures).
364   Careful inspection of Fig. 3 suggests that the strong and deep convective cells (black
365   contours in Fig. 3 indicate vertical velocity = 2 m/s at z = 6 km) are mainly located in the centers

366   of cold pool downdrafts, while new small cells are located at gust fronts where cold pools collide
367   (Fig. 3a). This behavior is consistent with the fact that cold pools are a consequence of
368   precipitating deep convection, and suggests that colliding cold pools are effective in triggering
369   new convection (e.g., Schlemmer and Hohenegger 2014; Feng et al. 2015; Haerter et al. 2019).
370   However, the earlier triggering of convection and colliding cold pools in DRY does not ensure a
371   stronger or more organized MCS at later stages. Instead, we see a better organized and longer-
372   lasting MCS in WET (Fig. 3c vs. Fig. 3f). Looking at the time evolution of convection in DRY
373   (Fig. 3a-c), the area with active convection is getting smaller throughout the afternoon and
374   evening. While gust fronts still exist in the later stage (Fig. 3c), most of them barely collocate
375   with deep convection. On the contrary, although deep convective cells are triggered at a later
376   time in WET than DRY, they eventually become better organized and stronger with time (Fig.
377   3d-f). Therefore, our simulations show the importance of surface energy partitioning for MCS
378   development, and that colliding cold pools alone are not sufficient to develop or sustain an MCS
379   when the environment is unfavorable.
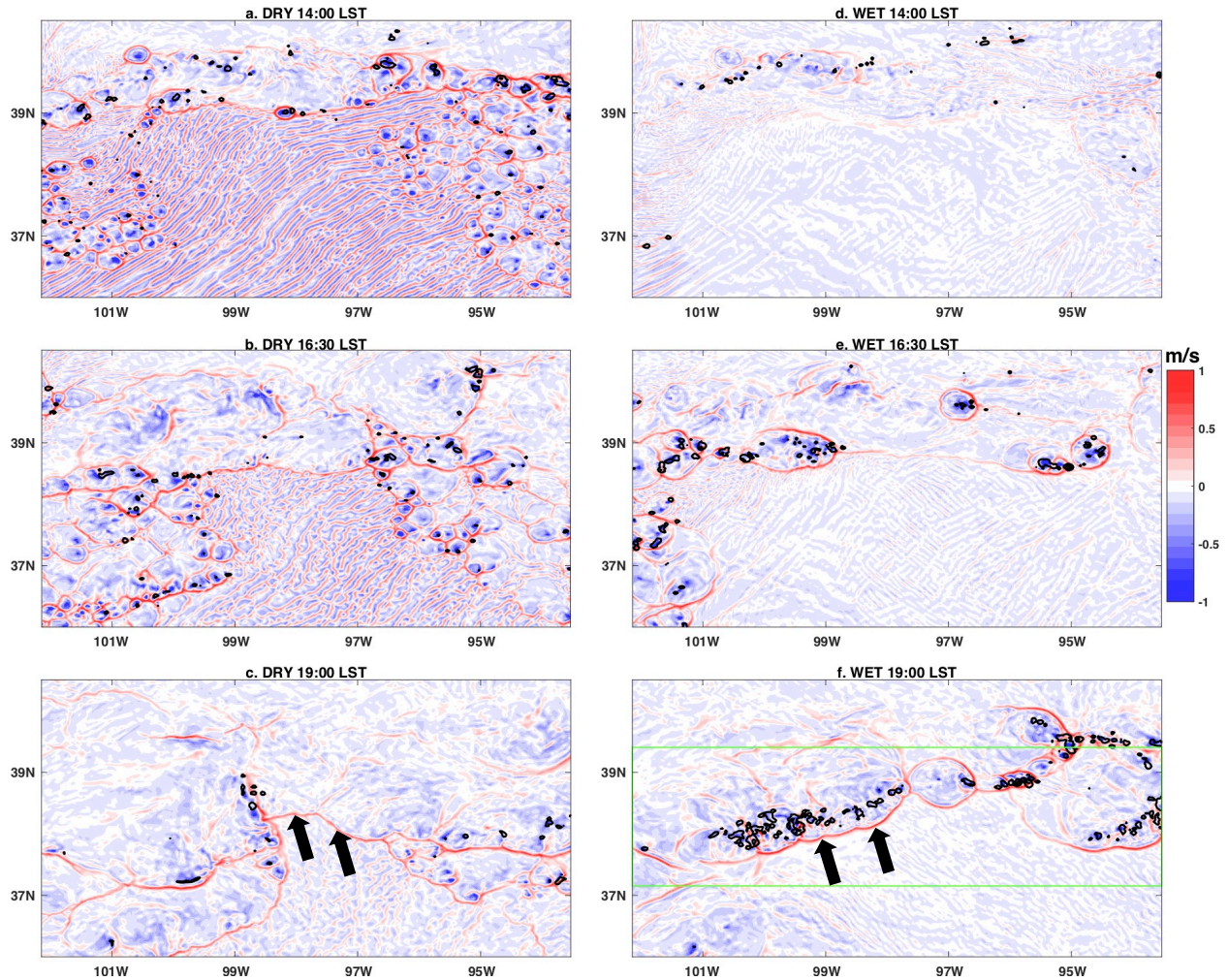
380
381   Figure 3. Time evolution of DRY (left panels) and WET (right panels) experiments for 2006-08-10 case. Shading is
382   vertical velocity (m/s) at z = 200 m, and black contours indicate vertical velocity of 2 m/s at z = 6 km. The green
383   box in f indicates the region used for moist static energy analyses shown below. Black arrows in c and f are
384   examples of locations of gust fronts.
385
386

4.1.1. MSE analysis

387
388 To address both the CAPE and entrainment mechanisms noted in the introduction, we analyzed
389 the moist static energy (MSE). Specifically, we hypothesized that the shallower PBL over the
390 wetter surface allowed MSE to accumulate in the PBL, providing more CAPE for mesoscale
391 circulations at later stages in WET (as in Schar et al. 1999). Fig. 4 shows the probability density
392 function (PDF) of the frozen MSE, which is defined as $MSE = C_pT + gz + L_vq_v - L_fq_i$, where
393 C_p is the dry air specific heat, T the temperature, L_v and L_f the latent heat of vaporization and
394 freezing, and q_v and q_i the specific humidities of water vapor and ice. The MSE is then divided
395 by C_p to have a temperature (K) unit. We use the frozen MSE because it is nearly conserved even
396 with the presence of ice phase change. We have chosen a relatively narrow subdomain (magenta
397 box in Fig. 3f) in order to minimize the effects of meridional temperature gradient. The chosen
398 subdomain contains most of the MCS as well as the environment.
399   Similar to Schar et al. (1999), the cooler surface in WET (energy is used to evaporate
400 water instead of heating the surface) makes a shallower boundary layer and less entrainment
401 mixing with the overlying atmosphere than DRY. This effect concentrates more MSE near the
402 surface, creating a sharper gradient in MSE across the PBL top in WET (lower panels of Fig.4)
403 compared to DRY (upper panels of Fig. 4), indicating larger CAPE in WET than in DRY. This is
404 partly due to less PBL-entrainment and mixing of surface enthalpy fluxes with the more stable
405 air above the PBL; but also the higher boundary layer q_v and lower air temperature by the wetter
406 soil moisture reduces the difference between the dewpoint and temperature (increased relative
407 humidity, not shown) in the boundary layer, causing a much lower LCL and LFC in WET than
408 DRY (the starting point of the entraining plume model to be shown below indicates the height of
409 LCL). At 14:00 LST, the area-mean (within the magenta box in Fig. 3f) CAPE in WET is about
410 4000 J/kg, while it is only about 500 J/kg in DRY. As a result, both the time evolution of MSE
411 (Fig. 4) and vertical mass flux (Fig. 5) indicate that WET has stronger convective organization
412 than DRY at later stages.
413   As an aside, it is worth noting that the vertical integral of MSE is slightly greater in WET
414 (not shown), so that weaker vertical exchange across the PBL is not the only factor in explaining
415 the higher near-surface MSE in WET. The change in energy partitioning from sensible to latent
416 cannot explain the higher integrated MSE, since sensible and latent heat contribute equally to
417 MSE. A simple analysis of the surface energy budget revealed that the net shortwave radiation
418 (downward) was nearly the same between WET and DRY, but the net longwave radiation
419 (upward) in WET was about 100 W/m^2 less than DRY, due to the colder surface temperature.
420 Also, the downward ground flux was about 100 W/m^2 larger in DRY than in WET, due to a
421 higher surface skin temperature in DRY. As a result, the net LH+SH in WET is about 200 W/m^2
422 higher than in DRY. Assuming this additional flux sustains for 6 hours in a 1000-m PBL, this
423 roughly gives an increase of MSE by about 4 K (MSE has a temperature unit in this paper). Note
424 that near-surface MSE in WET is more than 20 K larger than DRY (Fig. 4), much larger than 4
425 K. Therefore, the changed radiation and ground heat conductance in WET creates a secondary
426 yet significant apparent 'source' of MSE (more specifically, it is a reduction in heat losses to
427 radiation and conduction in WET compared to DRY). Also note that the radiation effect here is
428 different from that in Schar et al. (1999), where they referred to the more trapped longwave
429 radiation by convective clouds in WET than in DRY at later stages.
430
431
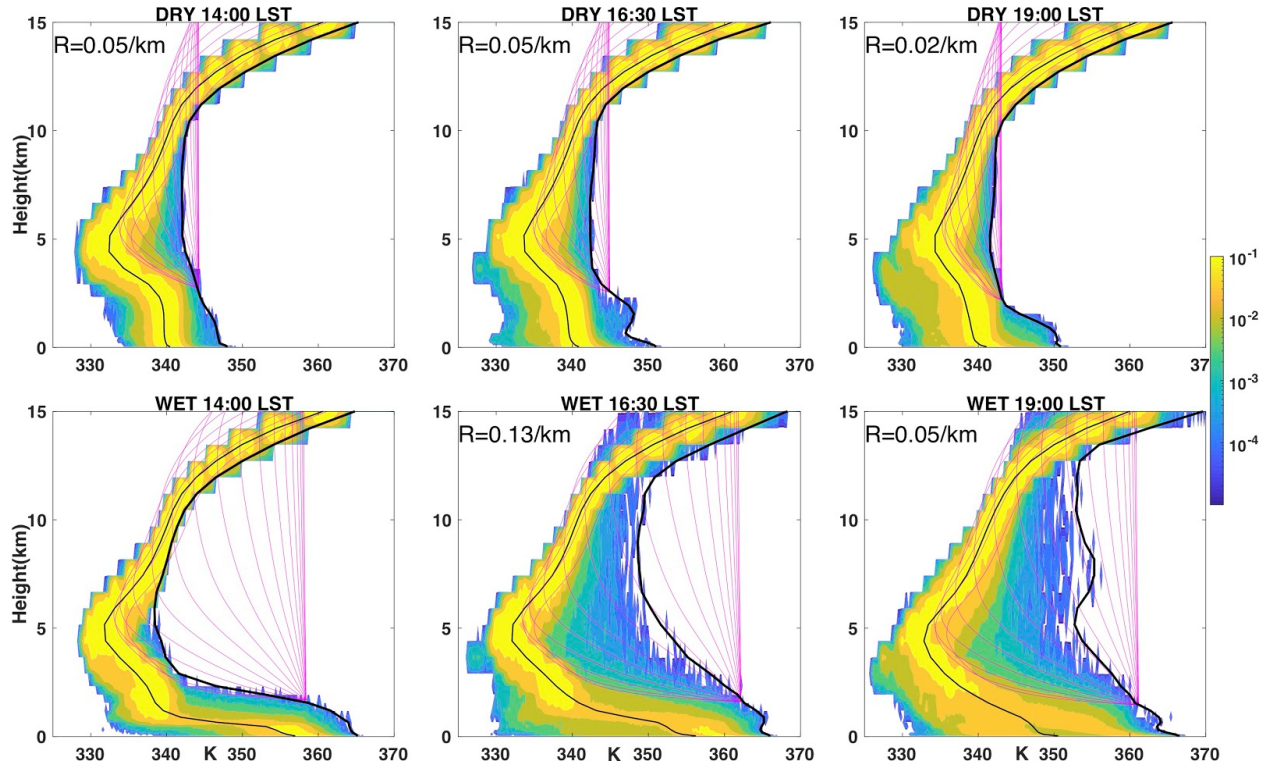
Figure 4. The time evolution of the probability distribution function (PDF, shading) of moist static energy (MSE, K) at each level for DRY (upper panels) and WET (lower panels). Thin and bolded black lines represent the domain mean and maximum MSE, respectively. The group of magenta lines in each panel represents the entraining plume model, where each line indicates the vertical MSE profile of a parcel decided only by a certain entrainment rate. The starting point of the parcel is at z = LCL and at the value of maximum MSE. Also shown in each panel is the entrainment rate fitted by the least squares of the maximum MSE profile between z = 3 and 10 km.
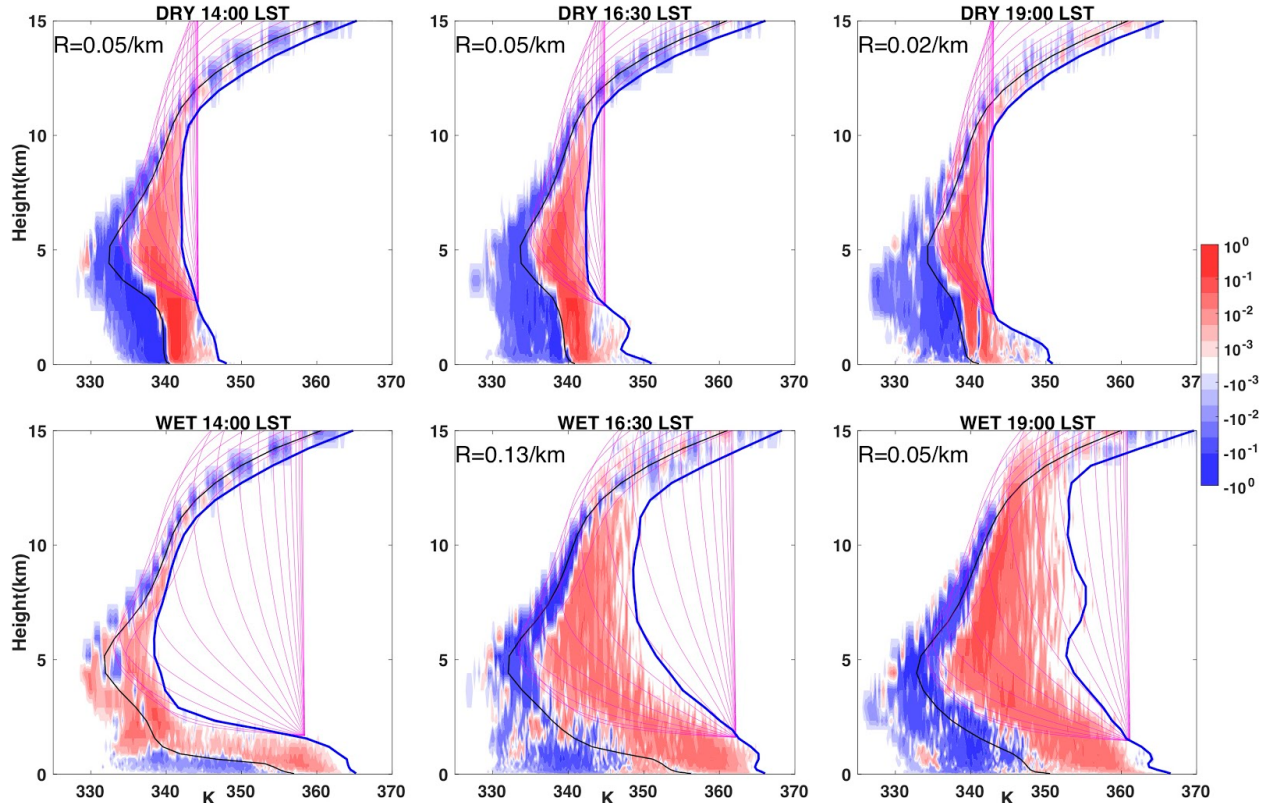
444
445 Figure 5. same as Figure4, except that the shading is the MSE-binned (0.2 K increment) vertical mass flux
446 normalized across panels so that the range of the flux is between [-1 1]. The bolded blue line represents the
447 maximum MSE.

448

4.1.2. Entraining plume model

450 A popular argument is that the cold pool can help organize convection by making clouds wider
451 and thus reducing their entrainment rate (e.g., Kuang & Bretherton, 2005; Khairoutdinov &
452 Randall, 2006; Schlemmer & Hohenegger, 2014). We want to see if this argument applies in our
453 case, and if entrainment plays a role in the better organization of convection in WET compared
454 to DRY. Here we followed the plume model method to estimate entrainment by Gentine et al.
455 (2016), where, for a given entrainment rate, the vertical gradient of MSE in a parcel is only
456 affected by the MSE difference between the parcel and the environment (similar to their Eq. 2) :
457 $\frac{\partial MSE}{\partial z} = R(\overline{MSE} - MSE)$, where $\overline{MSE}$ is the horizontal mean MSE to approximate environmental
458 MSE, R is the fractional entrainment rate, defined as the vertical gradient of the mass of cloud
459 parcel divided by the mass of cloud parcel. As a result, the vertical profile of the parcel MSE can
460 be uniquely defined (equation 3 of Gentine et al. 2016) for a constant entrainment rate:
461 $MSE(z) = (MSE(LCL)e^{R \cdot LCL} + \int_{LCL}^{z} R \cdot \overline{MSE}(z')e^{R \cdot z'} dz')e^{-R \cdot z}$. By trying several entrainment
462 rates one can estimate the rate as that which best fits a simulated profile. We defined the height
463 of the starting point as the mean LCL where clouds are present. The starting MSE was the
464 maximum MSE found at that LCL. The LCL was higher in DRY than in WET (as shown in Fig.
465 4 and Fig. 5), due to a warmer and drier PBL. The result of the plume model is shown in both
466 Fig. 4 and Fig. 5 as a group of magenta lines in each subplot. Each line represents a vertical
467 profile of MSE under one fixed entrainment rate. For example, the line where the MSE is
468 constant with height means that the entrainment rate is 0.

469   The main distinction between DRY and WET is that parcels start with higher MSE in
470   WET. In contrast, parcels in DRY start with an MSE value closer to the environment above the
471   PBL, reflecting the deeper and more entraining PBL in DRY than in WET. Parcels are subjected
472   to entrainment, reducing in-cloud MSE as they rise through the lower MSE air of the
473   environment. In WET, the reduction of in-cloud MSE is steeper at earlier times in the
474   development of the MCS, as inferred by the slope of the maximum MSE (thick blue lines in the
475   lower panel of Fig. 5), which suggests a decrease in the entrainment rate over time. We
476   quantitatively estimated the entrainment rate (R) by finding the value of R that predicts the best
477   fit to the 3-point running mean maximum MSE profile (between z = 3-10 km), using the least
478   squares method. R is systematically smaller in DRY than in WET at early times, as shown in Fig.
479   4 and Fig. 5. R further decreases slightly with time in DRY from 16:30 LST to 19:00 LST,
480   although cold pools and convection are only active in the early stage in DRY (between 14:00 and
481   16:30 LST, see Fig. 3a, b). In contrast, R starts higher but decreases with time in WET as the
482   convection in the MCS gets stronger (note that there is no value of R at 14:00 LST in WET
483   because of the lack of convection at that time in the region of interest). Recalling that cold pools
484   are more frequent (and colliding) early on in DRY and at later stages in the MCS evolution in
485   WET (as in Fig. 3), we conclude that these entrainment estimates are consistent with the idea that
486   cold pools help to reduce cloud entrainment by allowing wider, better organized clouds.
487   Therefore, the WET simulations support the idea that smaller entrainment rate with time
488   indicates convective organization with larger clouds. However, the rising parcels in DRY have
489   lower MSE and thus their profiles are less sensitive to entrainment due to similar in-cloud and
490   environmental MSE values. This suggests that the environment selects for wider or larger cloud
491   clusters (having lower entrainment rate) more so in WET than in DRY, such that entrainment
492   (and hence cold pools) may have less impact on cloud size distributions in DRY. This idea is
493   supported by cloud size distribution analyses at the end of Section 4.2.2 below.
494
4.2. The role of cold pools in MCSs
495
496   The cold pool is also hypothesized to have a significant impact on convective organization,
497   because the cold pool-induced gust front, especially by colliding cold pools, can effectively
498   trigger new convection (e.g., Rotunno et al., 1988; Schlemmer & Hohenegger, 2014; Feng et al.,
499   2015; Haerter et al., 2019), so that the MSC can be maintained. It is straightforward to think that
500   the stronger the cold pool evaporative cooling, the stronger the gust front, and the easier for new
501   convection to be triggered. This idea is manifested in recent cold pool parameterizations (e.g.,
502   Rio et al., 2009; Grandpeix & Lafore, 2010; Del Genio et al., 2015), in which the gust front
503   lifting ability is directly related to temperature deficits in cold pools. However, it needs to be
504   kept in mind that if the cold pool is too strong, newly triggered convective cells will be too
505   vertically slantwise or quickly detached from the surface source so that convection will be
506   suppressed (Rotunno et al. 1988). These two potentially offsetting effects of cold pools on
507   convection are key guidance for what is to be shown below.
508   As noted earlier, visual inspection of Fig. 3 shows more numerous cold pools in DRY at
509   the early stage (Fig. 3a) despite better organization and stronger convection in WET at the
510   mature stage (Fig. 3c). This indicates that the cold pool alone (without the environmental
511   condition) does not determine the fate of the MCS. To see what happens after convective
512   initiation, when the cold pool ceases to benefit convection, we examined both downdrafts and
513   updrafts, as well as their relationships. We might expect that stronger low-level downdrafts
514   would be coupled with stronger updrafts, in WET. To test this, we show the time evolution of the

515   frequency distribution of vertical velocity (W, m/s) in the boundary layer for WET and DRY.
516   The height of 250 m (upper panels of Fig. 6) was chosen to have clear signals of both cold pool
517   downdrafts and gust front updrafts, and samples were chosen where it was cloudy. Early on, at
518   14:00 LST, DRY (blue line in Fig. 6a) has a much broader distribution of low-level W than WET
519   (red line in Fig. 6a), simply because convection was triggered earlier in DRY. By 16:30 LST
520   (Fig. 6b), convection in WET had caught up with DRY in terms of updraft and downdraft
521   strength, per the wider distribution of W. However, considering all times together, peak low-
522   level downdraft and updraft strengths in WET were very similar to those in DRY (compare the
523   left-hand tails of the distributions of WET in Fig. 6b with those of DRY in Fig. 6a), suggesting
524   that cold pool gust fronts were not a driving factor in explaining the stronger and better-
525   organized MCS in WET. A look at mid-level updrafts gives yet another indication that gust
526   fronts alone do not explain the stronger convection in WET, since updrafts at 6 km are much
527   stronger in WET and the W distribution shows an asymmetric response at 6 km compared to that
528   at lower levels. These results suggest that surface energy partitioning, specifically its effect on
529   PBL state (vertical MSE profile) and CAPE, rather than cold pools, is responsible for the
530   convective development in WET at later stages. The persistence of relatively strong low-level
531   downdrafts at 19:00 LST in WET might in turn help sustain convection in WET, but appears
532   secondary to the favorable low-level thermodynamic environment created by the WET surface.
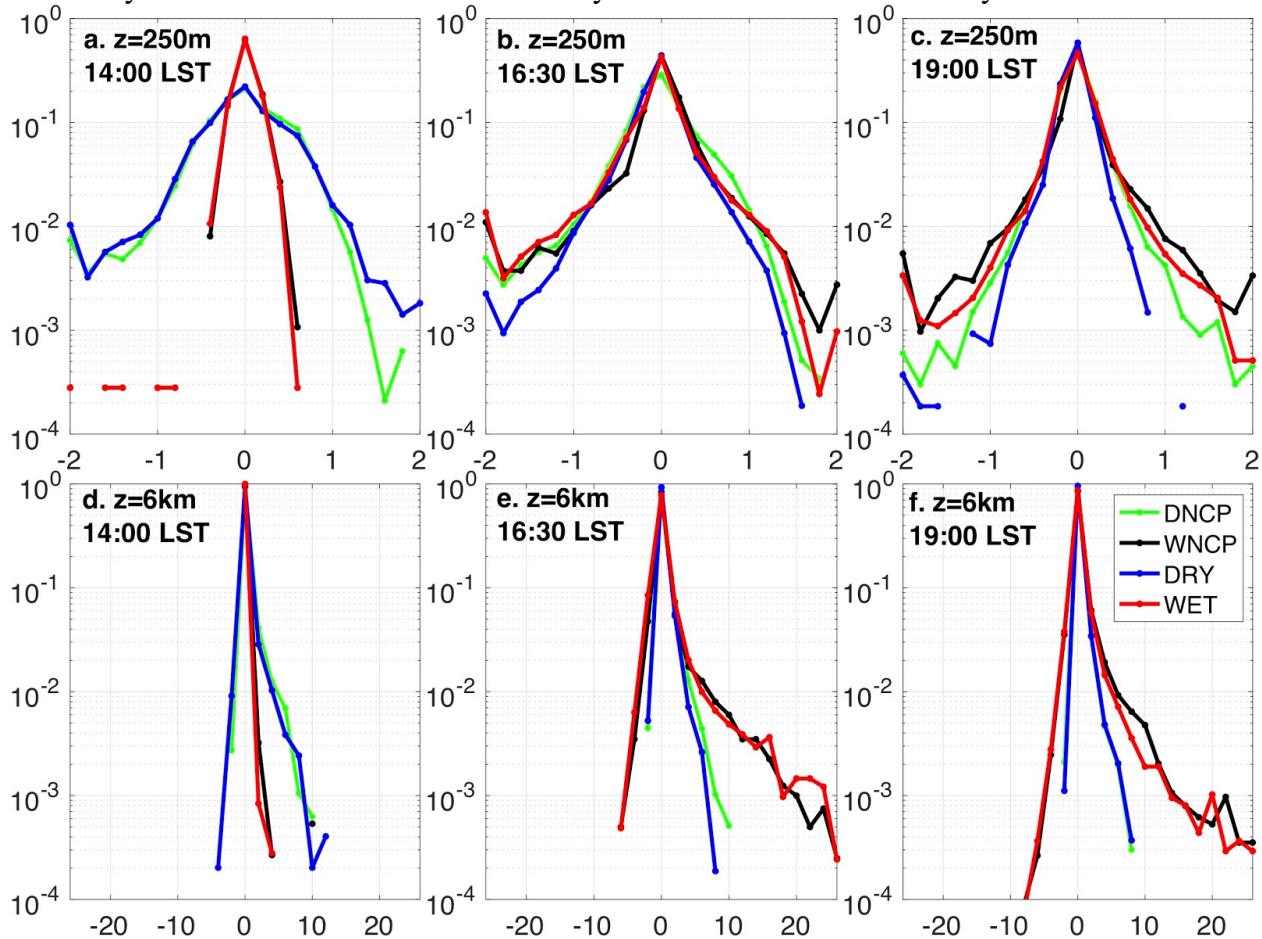
533
534   Figure 6. a-c. The relative frequency distribution of vertical velocity (m/s) at z = 250 m at 14:00, 16:30, and 19:00
535   LST for DRY (blue), WET (red), DNCP (green), and WNCP (black) simulations. b. Same as a, but for vertical

536 velocity (m/s) at z = 6 km. Logarithmic Y-axis is used for better visualization. 0 counts are not plotted due to the log
537 scale.

538

539

540 **4.2.1 "No-cold pool" experiments: Experimental setup**
541 To better clarify the role of cold pools in convective organization, we have performed "no-cold
542 pool" experiments by adjusting the Thompson microphysics. The most common way to remove
543 cold pools in model experiments is to turn off the evaporation of rain (such as Khairoutdinov &
544 Randall, 2006; Jeevanjee & Romps, 2013; Grant et al., 2018). That method should remove the
545 cold air, but downdrafts below the convective updrafts could still exist because the downward
546 dynamic pressure gradient force as well as hydrometeor loading effect is not removed. We have
547 removed the hydrometeor loading effect (together with turning off evaporation in microphysics)
548 in the vertical velocity equation, but found that the effect is minor when compared to
549 evaporation. Note that, due to the dynamic pressure gradient force, convective downdrafts cannot
550 be completely removed. Also, it is noteworthy that Rotunno and Klemp (1985) removed gust
551 fronts by preventing rain production in the idealized simulations. We have done similar
552 modifications, and found that their method is not feasible in realistic simulations with interactive
553 radiation because the cloud-radiation interaction creates a large area of very cold air (not shown).
554   Given the above discussion, we show the "no-cold pool" simulations where only
555 evaporation is turned off, so that other aspects of MCSs are as unaltered as possible. In order to
556 keep the microphysics near the updraft region as unchanged as possible, we only turn off
557 evaporation within the lowest 2 km, which is enough to "kill" most of the cold air in the cold
558 pool region. Turning off the evaporation for the whole atmosphere was also tested, and we found
559 similar results.

560

561 **4.2.2 "No-cold pool" experiments: Comparison to "cold-pool" simulations**
562 We ran "no-cold pool" experiments for both DRY and WET, hereafter named DNCP and WNCP
563 respectively. We collectively refer to the cold-pool and no cold-pool experiments as CP and
564 NCP. Even without rain-cooled air in the NCP simulations, gust fronts still exist (Fig. 7), but are
565 not as numerous as in the CP simulations (Fig. 3). The gust front horizontal propagation is faster
566 in CP than in NCP, which sweeps out a larger cold pool area and creates a larger area surrounded
567 by gust fronts (Fig. 3 vs. Fig. 7). Greater horizontal spread indicates a greater chance for gust
568 fronts to interact with the environmental air, and collide with each other. This is clear in the
569 middle stage of DRY (Fig. 3b vs. Fig. 7b) and WET (Fig. 3e vs. Fig. 7e; Fig. 3f and Fig. 7f),
570 where the total area of cold pools (surrounded by gust fronts) is larger in CP than NCP. We thus
571 confirm that one important aspect of the cold pool is to provide more gust fronts for convective
572 triggering and organization.

573
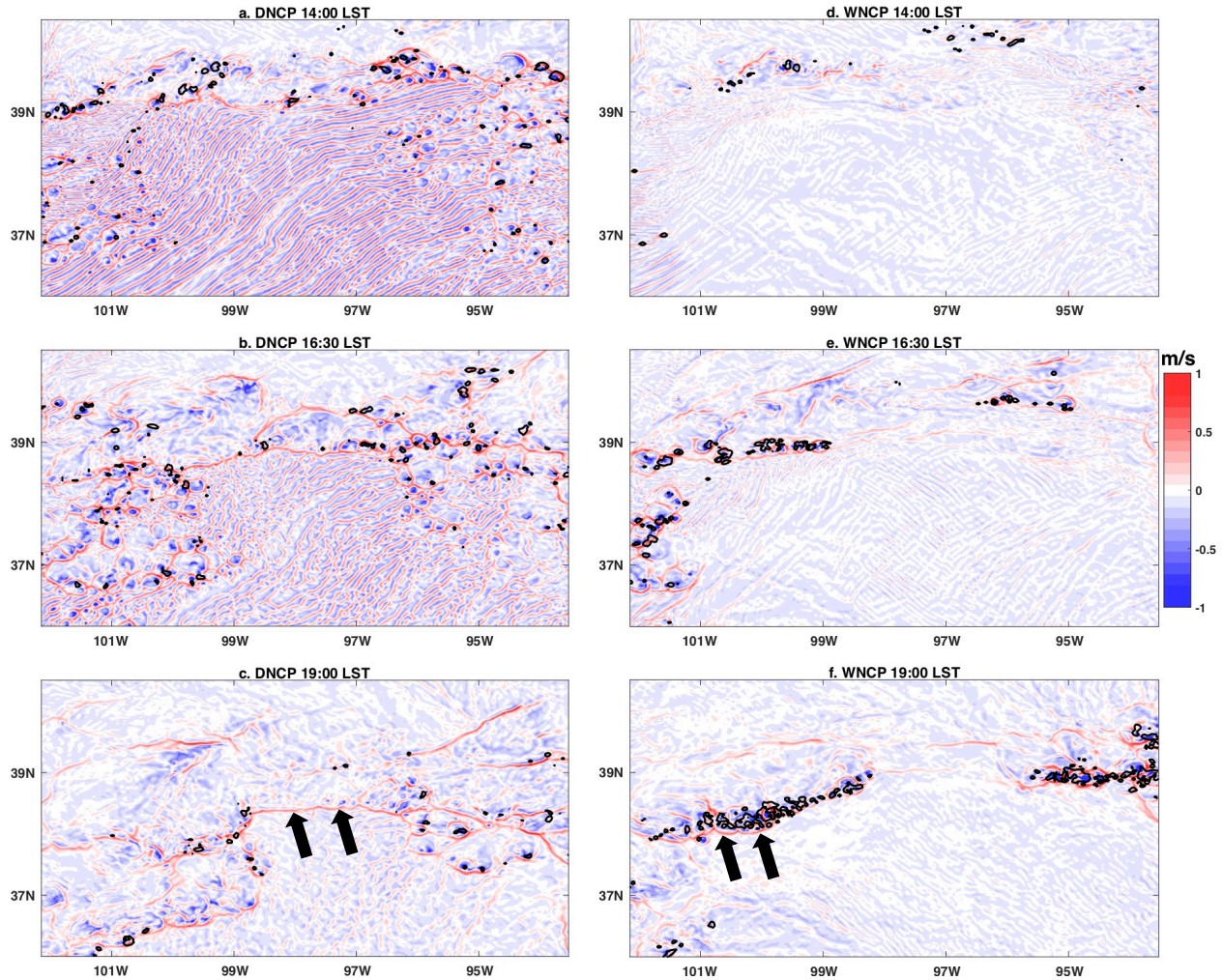
574
575   Figure 7. Same as Fig. 3, except for DNCP and WNCP simulations.
576

577   To check whether cold pools promote wider (less entraining) cloud clusters we compared
578   convective cell sizes (Fig. 8) between CP and NCP experiments. Deep convective cells were
579   defined where vertical velocity was larger than 0.7 m/s at z = 6 km. Data were separated into
580   small cells (radius ≤ 6 km, Fig. 8a) and large cells (radius > 6 km, Fig. 8b). Dry-soil experiments
581   had more small cells than wet-soil experiments (Fig. 8a), while the wet soil experiments had
582   relatively more large cells (Fig. 8b). Furthermore, there were more small cells in WET than in
583   WNCP, at all times (Fig. 8a), consistent with the hypothesis that vigorous cold pool gust fronts
584   and their collisions promote triggering of new cells. The sensitivity in the DRY/DNCP
585   experiments was limited to the early hours (14:00-16:30 LST) when convection is more active in
586   those simulations.
587   Counterintuitively, however, the NCP simulations had comparable or even more large
588   cells than CP (Fig. 8b). There were considerably more large cells in DNCP than in DRY, and
589   WNCP had the greatest number (number = 20) of large cells (between 14:00-19:00 LST).
590   Returning to the vertical velocity distribution (Fig. 6; black lines for WNCP, green lines for
591   DNCP) we also see stronger low-level (250 m; top panels of Fig. 6) downdrafts and updrafts in
592   NCP than in CP at 19:00 LST. The mid-levels (6km; bottom panels of Fig. 6) also show more

593   moderately-strong updraft (around 10 m/s) in WNCP than WET, at 16:30 and 19:00 LST,
594   indicating stronger convection in NCP simulations. Again, this is a bit counter-intuitive, because
595   stronger cold pools in WET should have resulted in stronger and better organized convection,
596   with larger cell sizes, unless something was working to offset or compete with that effect. Next,
597   we explore that offsetting effect, in the region where good convective organization was found
598   (the west part of Fig. 3f and Fig. 7f).
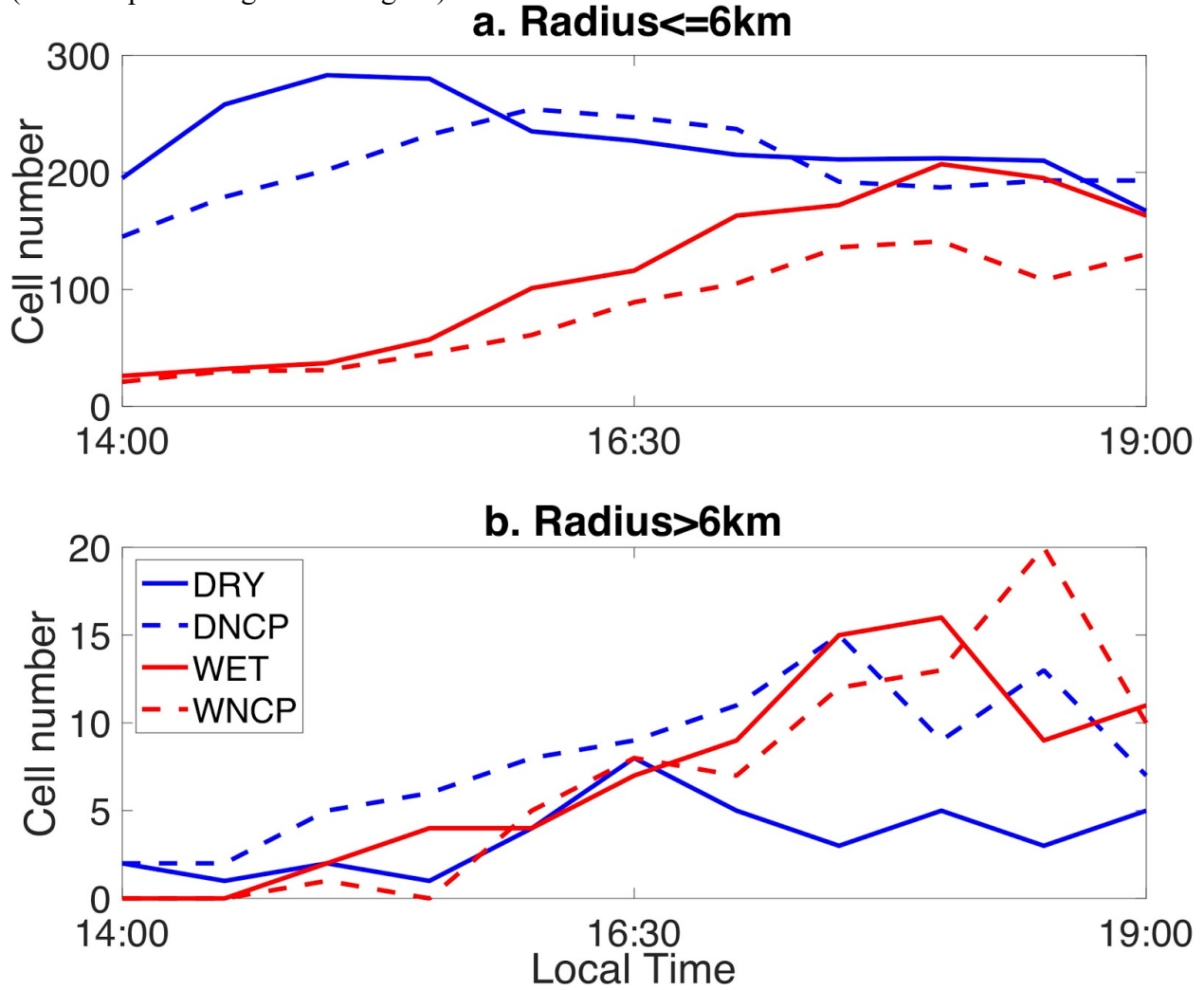
599
600   Figure 8. a. Time series of the number for small convective cells (radius ≤ 6 km) in each simulation. b. Same as a,
601   except for large cells (radius > 6 km).
602
603
604   **4.2.3 The offsetting effect of cold pools**

a. WET buoyancy 19LST

b. WNCP buoyancy 19LST
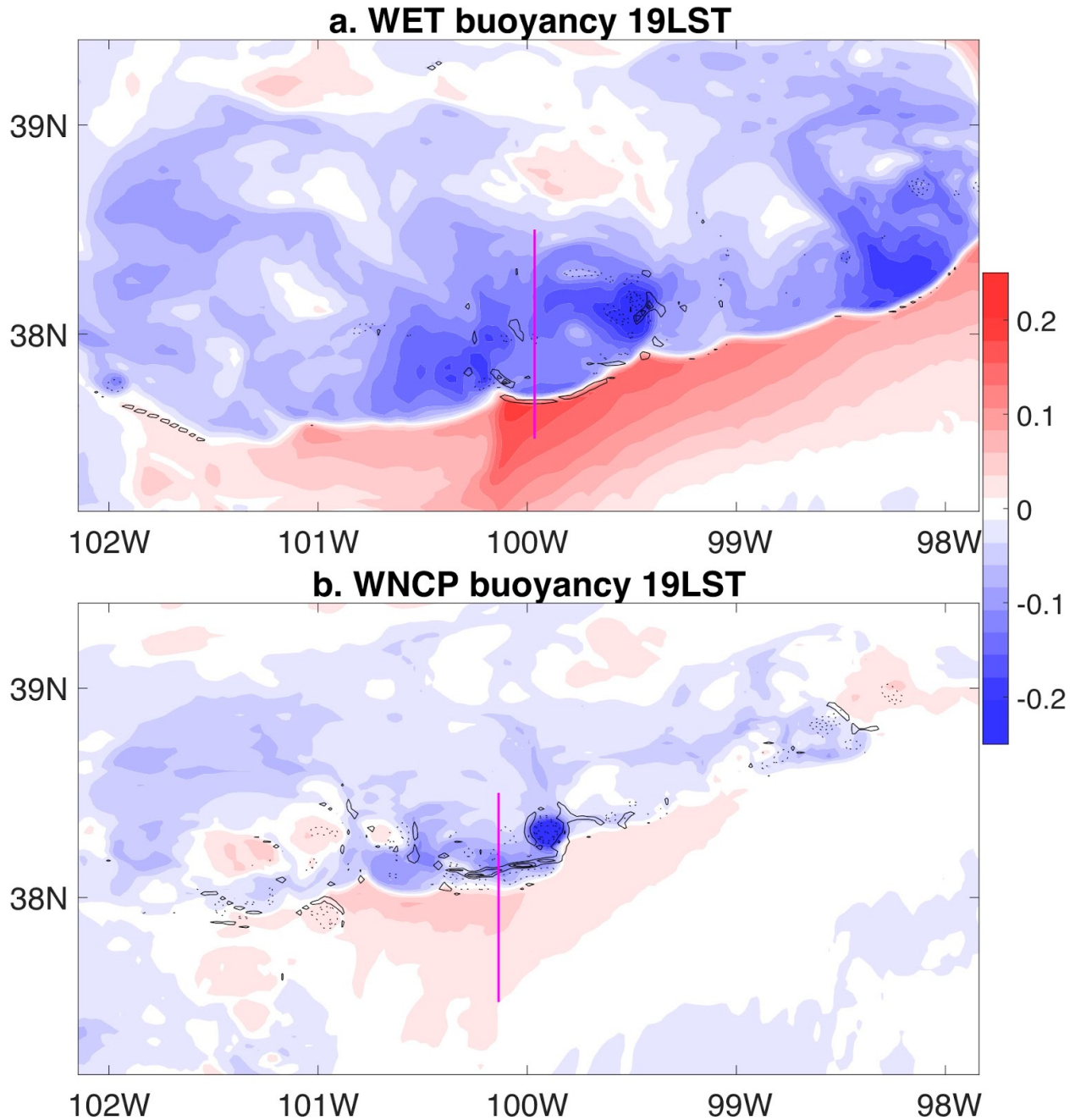
Figure 9. a. Buoyancy (shading, m s^{-2}, see definition in text) and divergence (s^{-1}, dashed contours are 0.003, 0.006, and 0.009; solid contours indicate convergence of -0.009, -0.006, and -0.003) in WET at t = 19 LST; Magenta line indicates the vertical cross section that is to be shown in Figure 10. b. same as a, except for WNCP.

Conceptually, we consider the horizontal propagation of the gust front separately from the strength of the horizontal wind itself. Namely, we note that the dense air in cold pools spreads laterally and pushes the gust front farther away from convective cores, while the downdraft brings higher momentum air downward and thus contributes to the strength of the horizontal wind gust. Hydrometeor loading and dynamic pressure gradient forces contribute to downdrafts, forming gust fronts even without evaporative cooling of rain, but they do not necessarily help to propagate the gust fronts horizontally beyond what is required by continuity of mass. Thus, the

617 horizontal propagation of gust fronts could be greater in CP compared to NCP due to the greater
618 density of the evaporatively-cooled air in CP, which may explain the weaker convective
619 updrafts/downdrafts and smaller cell sizes in CP. For example, in Rotunno et al. (1988), if the
620 cold pool is too strong, newly triggered convection becomes slanted toward cold pool side and
621 detached from the surface gust front.
622   We first verified that CP simulations indeed have denser cold pool air (lower or more
623 negative cold pool buoyancy) than NCP, which may not be obvious due to less hydrometeor
624 loading in CP simulations (from the removal of rain drops by evaporation). We used buoyancy
625 ($m\ s^{-2}$, shading in Fig. 9) to compare the low-level thermodynamics between WET and WNCP.
626 Similar to previous studies (such as Tompkins 2001 and Feng et al. 2015), buoyancy is defined
627 here as $B = g(\theta_\rho - \overline{\theta_\rho})/\overline{\theta_\rho}$, where the overbar is a running mean value from a 200 km by 200
628 km box centered on a given point, in order to get a local (relative) buoyancy given the large area
629 we are simulating (following Feng et al., 2015). θ_ρ is the density potential temperature (K)
630 defined as $\theta_\rho = \theta(1 + 0.608q_v - q_{cloud} - q_{rain})$, where θ is potential temperature, and q_v,
631 q_{cloud}, and q_{rain} represents the mass mixing ratios of water vapor, cloud droplets, and rain
632 water, respectively. Note that θ_ρ already includes the effect of hydrometeor loading. In
633 simulations where evaporation is not allowed, $(1 + 0.608q_v - q_{cloud} - q_{rain})$ in the cold pool
634 region will clearly decrease due to the decrease of water vapor and increase of hydrometeor
635 loading, given the same total water content. But it turns out that the enhanced θ (because no
636 evaporative cooling below z = 2 km) more than enough offsets the hydrometeor loading effect,
637 making θ_ρ in the "cold pool" region warmer, and creating a much weaker B in the "cold pool"
638 region in WNCP (Fig. 9b) than that in WET (Fig. 9a); note that we do find a small area of strong
639 negative buoyancy in WNCP, which is a result of very dense precipitation there.
640   Based on the above thermodynamic analysis, the much stronger negative B (denser air
641 cold pools air) in WET is indeed consistent with the faster horizontal gust front propagation in
642 WET compared to WNCP (Fig. 9a vs. Fig. 9b).
643   To see if the gust front propagation speed can explain the stronger, larger convective cells
644 in WNCP, we show a cross section of the secondary circulation (the meridional and vertical
645 wind) in Fig. 10. The vertical cross section was taken along the 99.9º W longitude line in WET
646 (100.1º W in WNCP), which is aligned nearly perpendicular to the gust front (indicated by the
647 magenta lines in Fig. 9). When cold pool downdrafts reach the surface, the strong horizontal
648 wind (yellow shading in Fig. 10) spreads over a larger horizontal distance (about 70 km) in WET
649 compared to WNCP (35 km). Since the cold pool air is much colder and denser than the
650 surrounding environment in WET than in WNCP, the cold air tends to intrude below the warm
651 air, instead of directly colliding with the warm air. The propagation of the gust front in WET is
652 thus 'too fast' such that newly triggered convective cells are detached horizontally from the old
653 convective cells that create the cold pool (red contours in Fig. 10a). The lifting of environmental
654 air behind gust fronts in WET follows a very slantwise trajectory upward (white line in Fig. 10a).
655 In contrast, the downdraft air and the environmental air in WNCP are forced almost directly
656 upward once they interact, because there is almost no density difference (Fig. 9b) between them.
657   We conclude that the more upright interface slope between the downdraft air and the
658 environment in WNCP (white line in Fig. 10b) explains why it has even more robust convection
659 than WET. The smaller distance between newly triggered and old convective cells in WNCP (red
660 contours in Fig. 10b) also favors stronger convection and possible merger of convection.
661
662
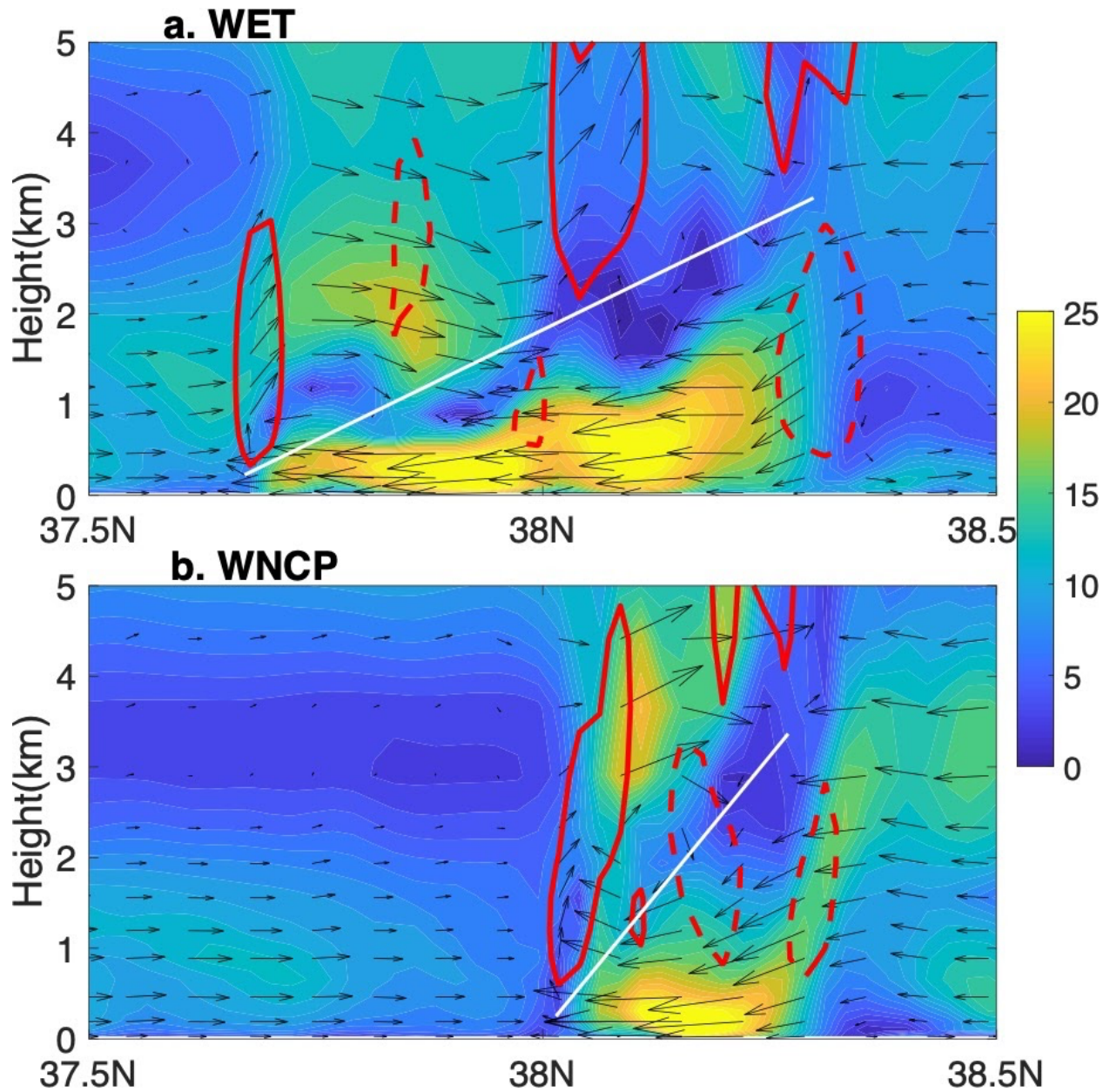
Figure 10. a. Vertical cross section of horizontal wind speed (shading) and secondary circulation at 19:00 LST (vectors indicate meridional wind V and vertical velocity W; note that W is multiplied by 2.5 for visualization). Red solid line indicates W = 2 m/s; red dashed line indicates W = -2 m/s. b. same as *a*, except for WNCP.
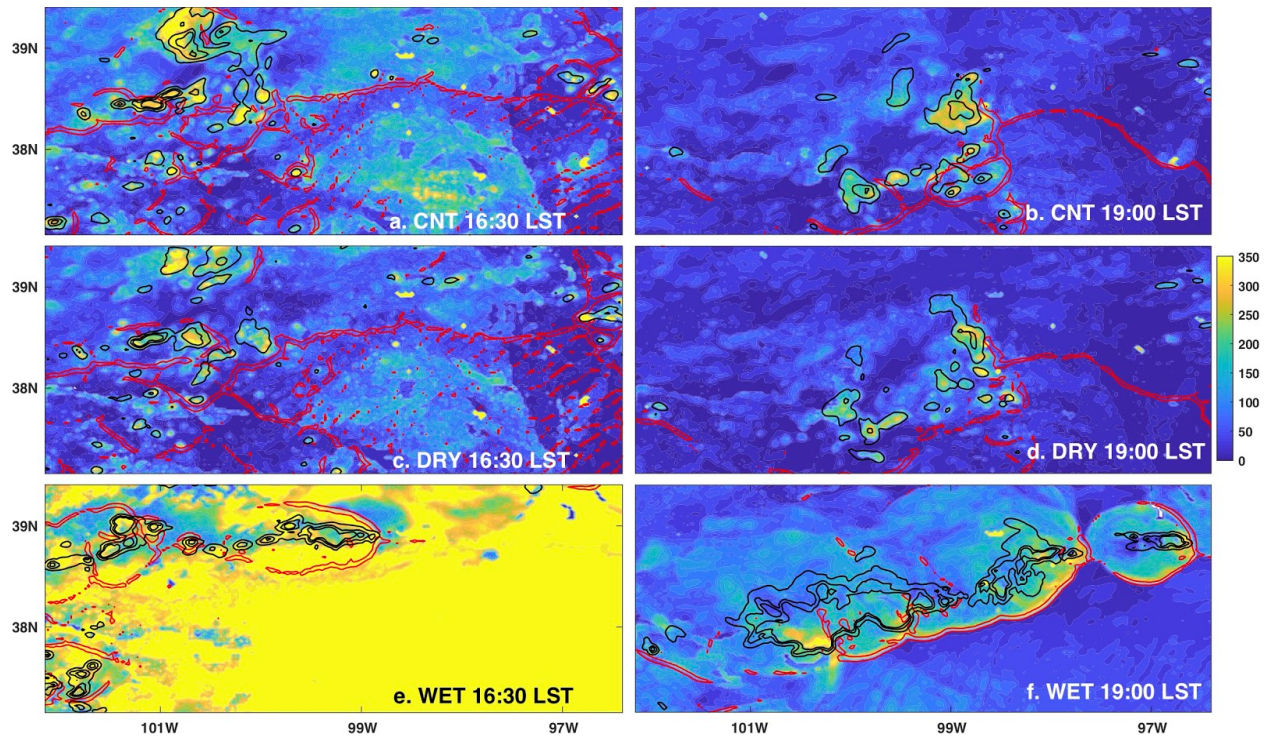
670
671 Figure 11. Surface latent heat flux distribution (shaded) for CTL (a and b), DRY (c and d), and WET (e and f), at
672 16:30 and 19:00 LST. Red contours represent vertical velocity of 0.5 m/s at z = 200 m to indicate gust fronts; Black
673 contours represent rain rates of 1, 5, and 10 mm/hour.
674
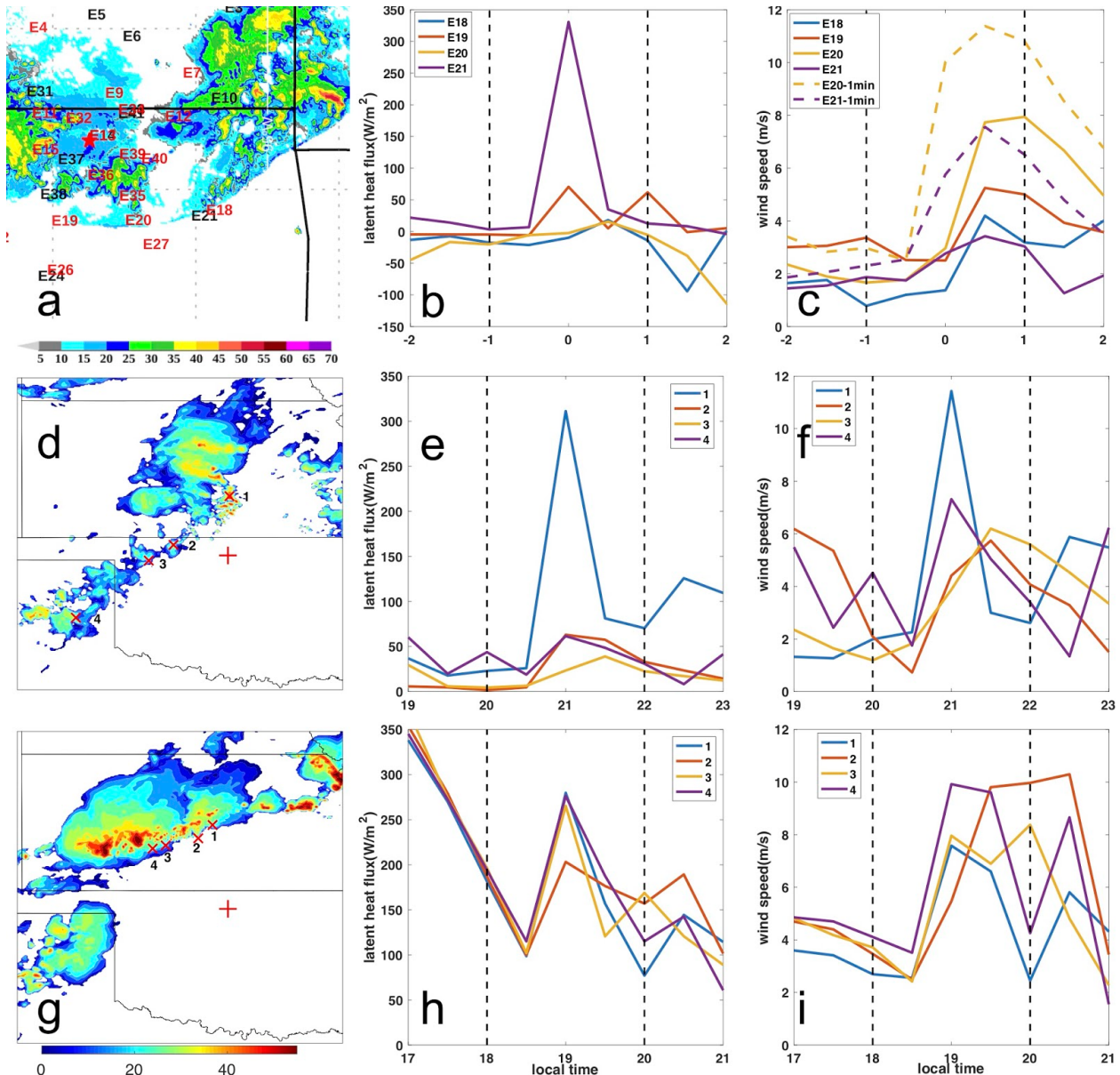
Figure 12. a. Radar reflectivity (dBZ) from NEXRAD at 21 LST on August 10th, 2006. Red star indicates the SGP main site. Red site labels indicate EBBR sites, while black labels indicate ECOR sites. b and c are the time series of latent heat flux and surface wind speed for site E18, 19,20, and 21. Time 0 indicates the passage of the gust front. The dashed lines in c are the maximum wind speed in every 30-minute interval using the MET 1-min data, for E20 and E21. The middle panels (d-f) are the same as the upper panels, except for model data in the control run (CTL) around 21 LST. Red crosses indicate the model grid points chosen for comparison to observations. Wind speed is calculated by 10-meter instantaneous U and V from the model output. The lower panels (g-i) are the same as the middle panels, except for model data in WET around 19 LST.

4.3 Surface wind and latent heat flux

Finally, we turn to the third mechanism of surface influence on convective organization, involving surface flux interactions. If an MCS is to persist beyond sunset, it must resist the detrimental effect of reduced (solar) energy available for surface sensible (SH) and latent heat flux (LH). As such, a positive feedback between surface LH and convection could be important for convective organization after sunset (note that we did not consider SH here, because SH was

691   much weaker than LH by late afternoon). Specifically, we ask: can cold pools and gust fronts
692   enhance the surface LH even after sunset when energy is limited?
693
694   **4.3.1 Latent heat flux in the model**
695   As expected, all simulations had weaker surface LH outside of the MCS region after sunset at
696   19:00 LST (right panels in Fig. 11) compared to 16:30 LST (left panels in Fig. 11). However, LH
697   within the gust fronts was still strong at 19:00 LST, particularly in WET (Fig. 11f). Thus, cold
698   pools and the associated gust fronts are able to enhance or maintain strong LH after sunset when
699   the atmospheric energy supply for evaporation is already limited. The LH at 19:00 LST within
700   the MCSs in CTL and DRY was also higher (comparable with that at earlier daytimes), but only
701   in areas near precipitation. We conclude that WET is most consistent with a positive feedback on
702   MCS growth, which would require the convection-enhanced surface LH to be spatially
703   correlated with new convection: most of the strong LH was located near leading gust fronts in
704   WET (red contours in Fig 11f), so that the LH could effectively feed back onto newly triggered
705   convective cells, making the MCS stronger and longer-lasting. Note that the high LH along the
706   gust front edge not only occur at 19:00 LST: it persists with time as gust fronts propagate (at
707   least in our 30-minute model output).
708
709   **4.3.2 ARM surface observations**
710   The surface observation network provides an opportunity to evaluate the model wind gusts and
711   to see whether the passage of the gust front is correlated with an enhancement of LH. In fact, a
712   gust front was captured in observations across the SGP site around 21:00 LST in the 2006-08-10
713   MCS case. A northeast-southwest gust front to the southeast of the SGP site (shown as the red
714   star in Fig. 12a) is clear around 21:00 LST in the radar maximum reflectivity from the NEXRAD
715   system (Fig. 12a). Four observational sites recorded this event, including three energy balance
716   Bowen ratio systems (sites E18, E19, and E20; all grassland sites) and one eddy-covariance
717   instrument (E21; an oak forest). Using the 4 sites, 30-min mean LH and near-surface wind speed
718   are plotted in Fig. 12b and 12c. We defined hour 0 as the time when the gust front passed each
719   site (around 19:00 LST at most sites, and 20:00 LST at site E19). Model surface wind speed was
720   taken from the instantaneous 10-meter wind output. We used observational data at 1-minute
721   temporal resolution where available (sites E20 and E21), and chose the maximum 1-minute wind
722   within each 30-minute range from the ARM Surface Meteorology Systems (MET) dataset, to be
723   consistent with instantaneous model output at the chosen grid cells near the gust front.
724   All sites showed an increase in LH as the gust front passed (Fig. 12b), although the
725   variation of the magnitude was large. E21 saw the largest increase (spike) in LH despite having
726   the smallest increase in wind speed, which may reflect higher canopy water vapor content at E21
727   relative to other sites (E21 is the only forested site here), as discussed further below. To show the
728   model surface wind and LH at scales similar to the observation, we chose three grid points (red
729   crosses in Fig. 12d) in the control run (CTL) along the gust front (points 2-4 in Fig. 12d); and
730   (for reasons given below) one additional point near convective cells with precipitation (point 1 in
731   Fig. 12d). Likewise, the lower panels of Fig. 12 show the results of WET at selected sites along
732   the gust front.
733   The spike in LH was similar in magnitude between observations and CTL (Fig. 12b, e) at
734   the time of gust front passage. However, in CTL the LH spike was confined to areas with
735   precipitation behind the gust front (model point 1), whereas it occurred along the gust front edge
736   in observations and in WET (lower panels of Fig. 12; and Fig. 11f). Thus, it is possible that the

737   model (CTL) is not able to represent the effect of land surface heterogeneity on surface heat
738   fluxes, while erroneously emphasizing the effect of precipitation 'recycling'. In particular, forest
739   canopy storage of water vapor is not represented in CLM, which may have limited the model's
740   LH along the gust front edge in CTL. However, whether this is the true physical explanation for
741   the observation at the E21 forest needs further investigation beyond this study.
742   Our results suggest that feedback of convection-induced wind gusts on surface LH could
743   be an important factor helping MCSs to persist after sunset. Both model and observation confirm
744   an enhancement of LH during passage of a gust front. Furthermore, the strong LH near gust
745   fronts (strong wind) instead of within cold pools (precipitation) is effective in supporting the
746   newly triggered convection, as seen in the WET simulation. This result provides a realistic case
747   to support earlier conclusions based on idealized model experiments, on the importance of
748   interactive surface heat fluxes (Gentine et al., 2016; Grant & Van den Heever, 2018).
749
750   **5. Discussion and Conclusion**
751   In summary, three main results were obtained on the roles of surface energy partitioning in
752   convective organization (MCSs) near the US SGP site: (1) Wetter soil (higher surface latent heat
753   flux relative to sensible) leads to a stronger MCS at later stages than drier soil in most of our
754   simulated cases, regardless of the earlier convective initiation in many of the drier soil
755   experiments; (2) although the cold pool helps trigger new convection, it can also offset
756   convection by making updrafts slantwise; and (3) cold pools allow MCSs to maintain large latent
757   heat flux (along leading gust-fronts) into nighttime.
758   Three possible mechanisms by which the cold pool could serve as an agent in the land-
759   convection coupling were explored: entrainment, ascent along gust fronts (particularly in high-
760   CAPE environments), and surface flux interactions. Entrainment rate was in general smaller in
761   DRY than WET, consistent with more numerous small cold pools (and their collisions) creating
762   larger clouds in the early afternoon in DRY. However, the build-up of MSE in the shallower
763   boundary layer in WET (and hence larger CAPE) becomes more important later in the MCS
764   development, ultimately favoring better organized MCSs in WET than DRY. Thus, while past
765   (smaller-domain studies) suggested that the cold pool collision is a main mechanism to promote
766   convection, our larger-domain study indicates that the large-scale modification of CAPE by
767   surface fluxes can ultimately determine the degree of convective organization and intensity at
768   later mature stages of the MCS. In addition, while the cold-pool-induced gust fronts provide the
769   uplift to trigger new convection, the dynamic (pressure perturbation) contribution to gust front
770   uplift makes this mechanism relatively insensitive to cold-pool density (negative buoyancy), as
771   discussed in further detail below. Nevertheless, the land-atmosphere difference created by cold
772   pool properties (dry, cold air, and strong gust-front wind) could help to increase or maintain
773   surface heat fluxes, potentially promoting convective organization.
774   Given what has been learnt about cold pools in this study, the cold pool parameterizations
775   can be potentially improved. In previous cold pool parameterizations, the gust front lifting ability
776   is proportional to the negative-buoyancy-induced horizontal propagation speed (or cold pool
777   intensity), which is associated with the evaporative cooling of hydrometeors (e.g. Rio et al.,
778   2009; Grandpeix & Lafore, 2010; Del Genio et al., 2015). However, strong cold pools might not
779   be as efficient to lift environmental air as calculated by these cold pool parameterizations,
780   because a slantwise interface slope between the density current and environment will
781   substantially weaken the gust front uplift, as seen in our CP and NCP comparisons. The interface
782   slope can be easily incorporated into the cold pool parameterizations by introducing a parameter

783 associated with the density difference between cold pool and environmental air. The slope may
784 explain the need for tunable parameters in cold pool parameterizations, which may need to be
785 modified to accommodate different microphysics schemes. For example, in Rio et al. (2009), the
786 lifting energy of gust fronts is only half of the wake potential energy (see their auxiliary
787 material), which might be a compromise of the slope of the updraft.
788   The enhancement of LH during the passage of a weak gust front at night in both the
789 model and observation suggests a positive feedback between surface fluxes and convective
790 organization. It may be noted that we focused only on locally forced MCSs in this study: many
791 simulated cases are less well-organized MCSs with more scattered convection, instead of 'text-
792 book' MCSs whose convection is stronger and more clustered. To what extent this local forcing
793 (surface energy partitioning) is important compared to other factors (such as low-level jet and
794 vertical wind shear) needs further investigation.
795   By resolving convection, the current simulations not only confirm previous findings (e.g.,
796 Schar et al., 1999; Findell & Eltahir 2003b) that more precipitation occurs over wetter soil, but
797 also emphasize that the resolved convective organization and cold-pool gust front are responsible
798 processes. How to accurately represent those processes in convection-parameterized climate
799 models is a persistent problem. In addition to the potential advantage by incorporating the
800 adverse (depending on environmental wind shear) effects of strong cold pools into cold pool
801 parameterizations, this study also suggests that the coupling between cold pools and the
802 interactive land surface could help convection persist into the night, and is worth further
803 exploring in terms of parameterization. Lastly, the role of cold pools on convection differs at
804 different stages, casting doubts on cold pool parameterizations that only focus on one aspect.
805 Thus, stage-dependent processes might be needed to represent cold-pool effects on convective
806 organization in Earth system models.
807
808

825 **References:**
826 Chen, S.-H. and W.-Y. Sun (2002). A one-dimensional time dependent cloud model. *J. Meteor. Soc. Japan.*, *80*(1),
827   99–118.
828

829   Dai, A., F. Giorgi, and K. E. Trenberth (1999). Observed and model simulated diurnal cycles of precipitation over
830   the United States, *J. Geophys. Res.*, *104*, 6377–6402, doi:10.1029/98JD02720.

831

832   Del Genio, A.D., J. Wu, A.B. Wolf, Y. Chen, M. Yao, and D. Kim (2015). Constraints on Cumulus Parameterization
833   from Simulations of Observed MJO Events. *J. Climate, 28*, 6419–6442.

834

835   Feng, Z., L. R. Leung, S. Hagos, R. A. Houze, C. D. Burleyson, and K. Balaguru (2016). More frequent intense and
836   long-lived storms dominate the springtime trend in central US rainfall. *Nat. Commun., 7*, 13429.

837

838   Feng, Z., S. Hagos, A. K. Rowe, C. D. Burleyson, M. N. Martini, and S. P. de Szoeke (2015), Mechanisms of
839   convective cloud organization by cold pools over tropical warm ocean during the AMIE/DYNAMO field campaign,
840   *J. Adv. Model. Earth Syst., 7*, 357–381.

841

842   Findell, K. L., and E A B Eltahir (2003). Atmospheric controls on soil moisture-boundary layer interactions. Part I:
843   Framework development. *Journal of Hydrometeorology*, *4*(3), 552-569.

844

845   Findell, K. L., and E A B Eltahir (2003). Atmospheric controls on soil moisture-boundary layer interactions: Three-
846   dimensional wind effects. *Journal of Geophysical Research*, *108*(D8), 8385.

847

848   Fritsch, J. M., R. J. Kane, and C. R. Chelius (1986). The contribution of mesoscale convective weather systems to
849   the warm-season precipitation in the United States. *J. Climate Appl. Meteor., 25*, 1333–1345.

850

851   Froidevaux, P., L. Schlemmer, J. Schmidli, W. Langhans, and C. Schär (2014). Influence of the Background Wind
852   on the Local Soil Moisture–Precipitation Feedback. *J. Atmos. Sci., 71*, 782–799.

853

854   Gantner, L., and N. Kalthoff (2010). Sensitivity of a modelled life cycle of a mesoscale convective system to soil
855   conditions over West Africa. *Quart. J. Roy. Meteor. Soc., 136*, 471–482.

856

857   Gentine, P., A. Garelli, S.-B. Park, J. Nie, G. Torri, and Z. Kuang (2016). Role of surface heat fluxes underneath
858   cold pools, *Geophys. Res. Lett., 43*, 874–883.

859

860   Gentine P, A. Holtslag, F D'Andrea , and M Ek (2013). Surface and Atmospheric Controls on the Onset of Moist
861   Convection over Land. *Journal of Hydrometeorology.* 14:1443-1462.

862

863   Grandpeix, J. and J. Lafore (2010). A Density Current Parameterization Coupled with Emanuel's Convection
864   Scheme. Part I: The Models. *J. Atmos. Sci., 67*, 881–897.

865

866   Grant, L. D., & van den Heever, S. C. (2018). Cold pool-land surface interactions in a dry continental environment.
867   *Journal of Advances in Modeling Earth Systems, 10*, 1513–1526.

868

869   Grant, L.D., T.P. Lane, and S.C. van den Heever (2018). The Role of Cold Pools in Tropical Oceanic Convective
870   Systems. *J. Atmos. Sci., 75*, 2615–2634.

871

872   Guillod, B., Orlowsky, B., Miralles, D. et al. (2015). Reconciling spatial and temporal soil moisture effects on
873   afternoon rainfall. Nat Commun 6, 6443. https://doi.org/10.1038/ncomms7443.

874

875   Haerter, J. O., Böing, S. J., Henneberg, O., & Nissen, S. B. (2019). Circling in on convective organization.
876   *Geophysical Research Letters, 46*, 7024–7034.

877

878   Houze, R. A., Jr. (1994). *Cloud Dynamics*. International Geophysics Series, Vol. 53, Academic Press, 573 pp.

879

880   Hohenegger, C., P. Brockhaus, C.S. Bretherton, and C. Schär (2009). The Soil Moisture–Precipitation Feedback in
881   Simulations with Explicit and Parameterized Convection. *J. Climate, 22*, 5003–5020.

882

883 Iacono, M. J., J. S. Delamere, E. J. Mlawer, M. W. Shephard, S. A. Clough, and W. D. Collins (2008). Radiative
884 forcing by long–lived greenhouse gases: Calculations with the AER radiative transfer models. *J. Geophys. Res.*, *113*,
885 D13103.

886

887 Jeevanjee, N., and D. M. Romps (2013). Convective self-aggregation, cold pools, and domain size, *Geophys. Res.*
888 *Lett., 40*, 994–998.

889

890 Jeevanjee, N. and D.M. Romps (2015). Effective Buoyancy, Inertial Pressure, and the Mechanical Generation of
891 Boundary Layer Mass Flux by Cold Pools. *J. Atmos. Sci., 72*, 3199–3213.

892

893 Khairoutdinov, M. and D. Randall (2006). High-Resolution Simulation of Shallow-to-Deep Convection Transition
894 over Land. *J. Atmos. Sci., 63*, 3421–3436.

895

896 Konings AG, GG Katul GG, and A. Porporato (2010). The rainfall-no rainfall transition in a coupled land-
897 convective atmosphere system. *Geophys Res Letters,* 37:L14401.

898

899 Koster, R. D., Suarez, M. J., Higgins, R. W., & Van den Dool, H. M. (2003). Observational evidence that soil
900 moisture variations affect precipitation. *Geophysical Research Letters, 30*(5), 1241.

901

902 Kuang, Z., and C. S. Bretherton (2005). A mass-flux scheme view of a high-resolution simulation of transition from
903 shallow to deep cumulus convection. *J. Atmos. Sci., 63*, 1895–1909.

904

905 Lawrence, D. M., et al., 2011: Parameterization improvements and functional and structural advances in Version 4
906 of the Community Land Model. *J. Adv. Model. Earth Syst.*, **3**, M03001.

907

908 Lu, Y., and L. M. Kueppers (2012). Surface energy partitioning over four dominant vegetation types across the
909 United States in a coupled regional climate model (Weather Research and Forecasting Model 3–Community Land
910 Model 3.5). *J. Geophys. Res.*, *117*, D06111.

911

912 Markowski, P., and Y. Richardson (2011). *Mesoscale Meteorology in Midlatitudes*. Vol. 2. Wiley-Blackwell, 430
913 pp.

914

915 Minnis, P., Nguyen, L., & Palikonda, R. (2008). Near-real time cloud retrievals from operational and research
916 meteorological satellites. *Remote Sensing of Environment*.

917

918 Nakanishi, M., and H. Niino (2009). Development of an improved turbulence closure model for the atmospheric
919 boundary layer. *J. Meteor. Soc. Japan*, *87*, 895–912.

920

921 Pfeifroth, U., R. Hollmann, and B. Ahrens (2012), Cloud cover diurnal cycles in satellite data and regional climate
922 model simulations, *Meteorol. Z.*, 21(6), 551– 560.

923

924 Rio, C., F. Hourdin, J.-Y. Grandpeix, and J.-P. Lafore (2009). Shifting the diurnal cycle of parameterized deep
925 convection over land, *Geophys. Res. Lett., 36*, L07809.

926

927 Qiu, S. and I.N. Williams (2020). Observational evidence of state-dependent positive and negative land surface
928 feedback on afternoon deep convection over the Southern Great Plains. *Geophysical Research Letters*, 47,
929 e2019GL086622.

930

931 Rotunno, R. and J. Klemp (1985) On the Rotation and Propagation of Simulated Supercell Thunderstorms. *J. Atmos.*
932 *Sci., 42*, 271–292.

933

Rotunno, R., J.B. Klemp, and M.L. Weisman (1988). A Theory for Strong, Long-Lived Squall Lines. *J. Atmos. Sci., 45*, 463–485.

Schär, C., D. Lüthi, U. Beyerle, and E. Heise (1999). The Soil–Precipitation Feedback: A Process Study with a Regional Climate Model. *J. Climate, 12*, 722–741.

Schlemmer, L. and C. Hohenegger (2014). The Formation of Wider and Deeper Clouds as a Result of Cold-Pool Dynamics. *J. Atmos. Sci., 71*, 2842–2858.

Skamarock, W. C., and Coauthors (2008). A description of the Advanced Research WRF version 3. *NCAR Tech. Note* NCAR/TN-475+STR, 113 pp.

Squitieri, B. J., and W. A. Gallus, 2016: WRF Forecasts of Great Plains Nocturnal Low-Level Jet-Driven MCSs. Part I: Correlation between Low-Level Jet Forecast Accuracy and MCS Precipitation Forecast Skill. *Wea. Forecasting*, 31, 1301–1323.

Tang, S., Xie, S., Zhang, M., Tang, Q., Zhang, Y., Klein, S. A., et al. (2019). Differences in eddy-correlation and energy-balance surface turbulent heat flux measurements and their impacts on the large-scale forcing fields at the ARM SGP site. *Journal of Geophysical Research: Atmospheres*, 124, 3301–3318.

Taylor, C. M., R. A. M. De Jeu, F. Guichard, P. P. Harris, and W. A. Dorigo (2012). Afternoon rain more likely over drier soils, *Nature,* 489, 423–426

Thompson, G., P. R. Field, R. M. Rasmussen, W. D. Hall (2008). Explicit Forecasts of Winter Precipitation Using an Improved Bulk Microphysics Scheme. Part II: Implementation of a New Snow Parameterization. *Mon. Wea. Rev.*, *136*, 5095–5115

Tompkins, A.M. (2001). Organization of Tropical Convection in Low Vertical Wind Shears: The Role of Cold Pools. *J. Atmos. Sci., 58*, 1650–1672

Torri, G., Z. Kuang, and Y. Tian (2015). Mechanisms for convection triggering by cold pools, *Geophys. Res. Lett., 42*, 1943–1950, doi:10.1002/2015GL063227.

Williams, I. N. (2019). Evaluating soil moisture feedback on convective triggering: Roles of convective and land-model parameterizations. *Journal of Geophysical Research: Atmospheres, 124*, 317–332.

Williams, I.N., J. Lee, J. Tadic, Y. Zhang, and H. Chu (2020). Modeling spatial heterogeneity in surface turbulent heat flux in the US Southern Great Plains, *Journal of Geophysical Research: Atmospheres, 125*, e2019JD032255.

Yang, G. and J. Slingo (2001). The Diurnal Cycle in the Tropics. *Mon. Wea. Rev., 129*, 784–801.

Yin, J., J. D. Albertson, J. R. Rigby, and A. Porporato (2015). Land and atmospheric controls on initiation and intensity of moist convection: CAPE dynamics and LCL crossings. *Water Resources Research*, 51, 8476–8493.

Yin J, A. Molini, A. Porporato (2020). Impacts of Solar Intermittency on Future Photovoltaic Reliability. *Nat Communication* 11.

Zeng, D., X. Yuan, and J. K. Roundy, 2019: Effect of Teleconnected Land–Atmosphere Coupling on Northeast China Persistent Drought in Spring-Summer of 2017, *Journal of Climate*, 32, 7403-7420.